UNIVERSITÀ DEGLI STUDI DI CATANIA
Dipartimento di Fisica e Astronomia
International PhD in Nuclear and Particle Astrophysics
XXVIII Ciclo

---

Mariachiara Falco

# ANALYSIS OF HIGH RESOLUTION OBSERVATIONS OF SUNSPOTS FINE STRUCTURES

---

Tesi di Dottorato

---

Coordinatore: Prof. S. Romano

Tutor: Chiar.ma Prof.ssa F. Zuccarello

Cotutors: Dott. P. Romano
Dott. S. L. Guglielmino

---

anno accademico 2014/2015

# Contents

# Abstract

This Ph.D. thesis deals with the study of the interaction between plasma and magnetic fields on the Sun. Observations acquired during two observing campaigns, one at the Solar Swedish Tower and the other at the Richard B. Dunn Solar Telescope, provided high-resolution data which were used to study the details of some phenomena occurring in the Sun. In particular, this work aims to extend and consolidate our knowledge on the formation and evolution of sunspots observed in the solar photosphere. The first aspect which was investigated concerns the study of the mechanism of the penumbra formation in a sunspot. In this regard, I give my contribution in explaining the behaviour of the magnetic field forming the penumbral filaments. A second aspect concerns the study of the kinematic and magnetic properties of a light bridge separating into two parts the umbra of a sunspot. I found that there is a relationship between the upflow motions in the light bridge dark lane and the magnetic field configuration. The third aspect concerns the study of the properties of granules in a light bridge and in the quiet Sun using a new algorithm developed in collaboration with the Department of Mathematics of the University of Catania. In particular, I compared the size, mean continuum intensity and Doppler velocity between the granules forming the light bridge and those of the quiet Sun. In the conclusion, I give my interpretation of the observed phenomena and suggest future observations to confirm these results and support theoretical models.

**Keywords:** *Sun, photosphere, sunspots, granulation, light bridge, magnetic field, high resolution observations.*

# Introduction

The Sun is one of the most fascinating and studied objects of the sky. Our ancestors realized that our lives depend upon the Sun because it is a source of light and heat for the Earth. Nowadays the study of the Sun has different aims: we try to understand how the Sun works, why it changes, and how these changes influence our planet. The Sun also plays an important role in helping us to understand other astrophysical objects.

Thanks to the relative proximity between the Earth and the Sun, we are able to observe in detail its atmosphere and so it is the key to understand other stars. Moreover, the progress in the area of the physics that studies the interaction between plasma and magnetic fields, called magnetohydrodynamics, is improving thanks also to the study of the Sun and the phenomena that occur in our star. On the Earth the plasma is present only in lightenings and aurorae, while in the Universe about 99% of the matter is in the state of plasma, such as: the Sun, the stars and the nebulae. The magnetic field is a crucial ingredient in the Sun, in fact there would not be sunspots, flares, prominences and coronal loops without the presence of the solar magnetic field.

One of the most remarkable phenomena of the solar magnetic activity are sunspots. They are a typical example of interactions between a plasma and a magnetic field. The formation of sunspots seems to be due to the emergence of magnetic flux tubes from the convection zone, but there are some aspects of this process which are not yet clear. Solar physicists believe that the emergence of the magnetic fields inhibits the process of energy transport from the convective zone, and this leads to the local cooling of the solar photosphere. Understanding the formation, evolution, dynamics and magnetic structure of sunspots is therefore a key to disentangle the basic physical processes taking place in the solar photosphere.

In the last decades, the knowledge of the Sun improved thanks to the new generation of space-based solar observatories. Some of the most important satellites aimed at performing solar observations are: Skylab, Solar Maximum Mission, SOHO (SOlar and Heliospheric Observatory), TRACE (Transition Region And Coronal Explorer), Hinode and SDO (Solar Dynamics Observatory). However, to study small features of the Sun, ground-based telescopes are also required. In fact, large ground based telescopes such as the Swedish 1-m Solar Telescope (SST), the Dutch Open Telescope (DOT), the GREGOR in Canary Islands and the Richard B. Dunn Solar Telescope (DST) in New Mexico allow to reach high spatial, spectral and temporal resolution.

The observing campaigns carried out at the ground-based telescopes, often jointly with satellite observations, can acquire a large number of data necessary to study our star.

In this thesis I analyze some datasets obtained during two observing campaigns in order to investigate three different aspects of the sunspot formation and evolution.

The first aspect is the formation of the penumbra in a sunspot. This is a common phenomenon in solar active regions, but there are few observations of this process that are characterized by high spatial, spectral, and temporal resolution. Therefore, many open questions about the penumbra and its formation are still unanswered. It is not clear what is the crucial ingredient that initiates the transformation from a pore into a sunspot with a full-size penumbra, and also where the magnetic flux that is needed to form the penumbra comes from. The event of flux emergence together with the formation of sunspots represents a crucial episode of the full problem. In this scenario, I reached the conclusion that the magnetic canopy overlying the region surrounding the umbra at the chromospheric level may play an important role in the formation of the penumbra in the photosphere (Romano et al., 2014).

The second aspect that is analyzed in this work deals with the structures called light bridges, which appear inside the umbra of a sunspot during its coalescence process or during its fragmentation. Light bridges can have various shapes, intensities, and size and their classification is still not unambiguous. Recent studies suppose that the light bridges are deep formed structures created by field-free (or weak-field) plasma intruding into an otherwise magnetic sunspot and recent researches concerning light bridges are focused on their magnetic field and plasma motions. In this thesis I report the study of the plasma motions in a light bridge surrounded by two different magnetic field configurations. I found an interesting relation between the magnetic field and the upflow motions in the dark lane of the light bridge studied. These results are described in detail in Falco et al. (2015a).

The third studied aspect concerns the difference between the granules in a light bridge and those observed in the quiet Sun. Recently, the study of the solar granulation has been done by different authors with different kind of observations. The method used to identify a single granule changes in different studies, as well as the results obtained. Open questions concerning the lifetime, size and plasma motions of granules in the light bridges still need an answer and the way of formation and evolution of the granules is under investigation. In this context, I applied a new algorithm, developed in collaboration with the Department of Mathematics of the University of Catania, to identify the granules forming a light bridge and those of the quiet Sun, studying the differences in size, mean continuum intensity and mean Doppler velocity. The application of the new identification algorithm to my dataset shows that the granules of the LB are characterized by lower values of the diameter, intensity and Doppler velocity with respect to the values measured in the granules of the quiet Sun. I found that some of the results obtained do not confirm previous finding reported in literature. The results obtained in this work are described in Falco et al. (2015b).

This thesis is organized as follows:

- in chapter 1 a description of the different, often contradictory, results of previous investigations on solar photospheric features (i.e., granulation and sunspots with their fine structures) is given;
- in chapter 2 the instruments used to acquire the datasets analyzed in this work are described;
- chapter 3 describes the study of the penumbra formation and in particular it deals with the so-called annular zone above a pore, where the penumbra is forming during the observation interval;
- in chapter 4 the study of a light bridge in a decaying sunspot is reported. I study maps of temperature, Doppler velocity and inclination angle of the magnetic field in a light bridge;
- chapter 5 deals with the description of a new algorithm for the study of the solar granulation. In this chapter the different physical properties of the quiet Sun granulation and of the granules forming a light bridge are described;
- at the end of this work I draw my conclusions on the different aspects studied and I provide some hints for future observations and researches.

# Chapter 1

# The solar photosphere: granulation and sunspots

## 1.1 Solar granulation

The solar granulation is one of the most prominent manifestations of the convective motions occurring in the subphotospheric layers (see Figure 1.1). In particular, high resolution observations show that the solar surface is covered by a pattern of bright cellular elements called granules, surrounded by a network of dark intergranular lanes. What we see is the convective overshoot of the heat gas flow from the solar convection zone into the atmosphere. The organization and evolution of the granular cells in the solar photosphere reflects the physics of the upper convective layers of the Sun, but have also effects on higher layers, tranferring energy and momentum (Muller, 1999).

On the other hand, numerical simulations of solar granulation performed by Stein & Nordlund (1989, 1998) show that the granular pattern is mainly a surface phenomenon, driven by effective radiative cooling in the photosphere.

Statistical analyses have been carried out to understand the behaviour of the solar granulation and their results support the hypothesis

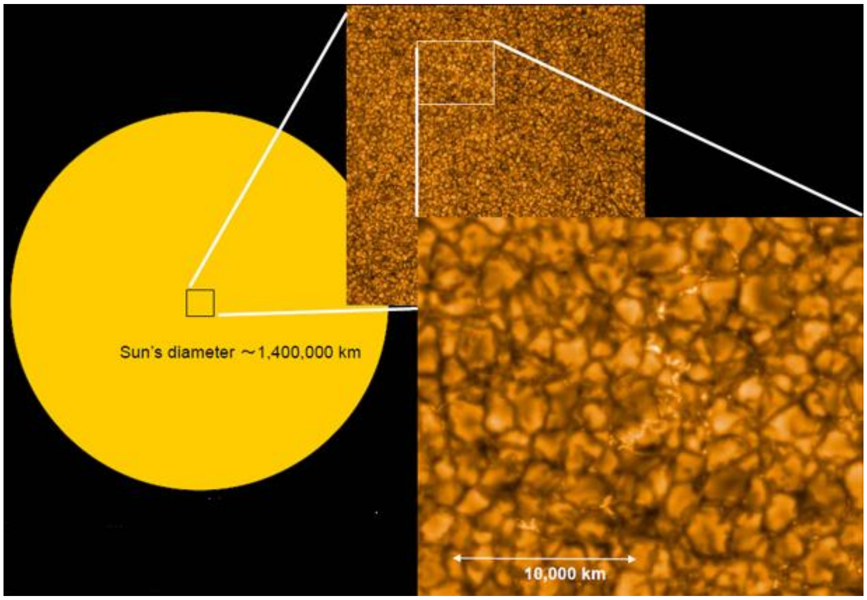

Figure 1.1: Detailed image of solar granulation acquired by the Hinode satellite.

that the solar granulation is produced by two interacting physical processes instead of being one single phenomenon: large-scale mechanisms, such as convection, and small-scale mechanisms, such as turbulence. Moreover, the geometric and thermodynamical properties are strongly dependent on the spatial scale of every single granule (Hirzberger et al., 1997).

The main problems in the study of solar granules are: i) the necessity of high resolution observations due to the small size of the granules (of the order of few arcseconds) and ii) the identification of the single granule, which depends on the algorithm used. Different approaches for the segmentation of solar features are reported in literature, starting from Roudier & Muller (1987), Hirzberger et al. (1997, 1999a,b), Strous (1995), Bovelet & Wiehr (2001) to the more recent algorithm presented by Berrilli et al. (2005).

The observed size of granules in the quiet Sun covers a range from approximately $0''.2$ to $3''.4$ (Brandt, 2001). Bray & Loughhead (1977) found a mean cell size of $1''.94$. According to Bray et al. (1984) the mean granular size amounts to $1''.35$ (excluding the surrounding dark lanes). Other studies carried out by Roudier & Muller (1986) found a mean cell size of $1''.76$. Moreover, Hirzberger et al. (1997) studied the granules area and found that granules with diameters smaller than $2''$ show regular shapes and an intensity increasing with the cell area, while granules larger than $2''$ are much more irregular and show a very weak variation of their mean and maximum intensities.

A study of the brightness of the solar granulation has been done by Hirzberger (2002) who found that the mean intensity distribution in a granule is between 0.85 $I_c$ and 1.15 $I_c$, with an average value at 0.998 $I_c$. The granular relative intensity with respect to the mean intensity in the quiet Sun was also studied by Jin et al. (2009). They found that some granules are darker than the mean photosphere and that the relative intensity of granules spans the range from 0.97 $I_c$ to 1.14 $I_c$, with a peak distribution at 1.07 $I_c$.

Jin et al. (2009) showed that the granular motion ranges from $-3.3\,\mathrm{km\,s^{-1}}$ (blueshift) to $2.0\,\mathrm{km\,s^{-1}}$ (redshift) with a peak at $-1.0\,\mathrm{km\,s^{-1}}$. Lagg et al (2014) found that in quiet Sun granules the upflow velocities in the interiors of the granules reach the maximum value of $-2.0\,\mathrm{km\,s^{-1}}$ in the deepest layers and $-1.0\,\mathrm{km\,s^{-1}}$ in the top layer.

According to Hirzberger (2002) the Doppler velocities of the granules in the quiet Sun seem to be symmetrically distributed around zero covering a range between $\pm1.5\,\mathrm{km\,s^{-1}}$ with a peak at $-0.15\,\mathrm{km\,s^{-1}}$. The slope towards negative velocities is significantly steeper than towards positive velocities. Moreover, the intensity and the velocity distribution within the granules depend on the granular size: in small granules the maximun intensity and maximum upward velocity are located close to the granular barycenters, while in large granules the brightest parts and maximum upward velocity are shifted towards the granular boundaries (Hirzberger, 2002).

Solar granulation studies pointed out that the granulation phenomenon is quite well understood, but its interaction with the magnetic fields needs a more detailed study. According to numerical simulations of magnetoconvection (Weiss et al., 1996; Blanchflower et al., 1998), the convective cells are prevented from expanding in presence of a magnetic field concentration (i.e., inside the umbra of a pore or sunspot). Indeed, in presence of a lower field strength, the magnetic field is dominated by the convective flow and the growing convective cells push the magnetic field into narrow lanes that surround them.

## 1.2 Sunspots

A great number of naked eye observations of sunspots are reported in Oriental (China, Korea and Japan) historical sources, but also in European, Arabic, Indian and Maya sources. The first known observation of a sunspot using a camera obscura was done by Kepler in 1607, but the beginning of the systematic study of the Sun started with the rediscovery of sunspots by Galilei, Scheiner and other around 1611, with the help of the newly invented telescope (Solanki, 2003; Vaquero, 2007). In 1612 during the summer months, Galileo made a series of sunspot observations which were published in *Istoria e Dimostrazioni Intorno Alle Macchie Solari e Loro Accidenti*, published in 1613. In Figure 1.2 a short sequence of the Galileo's sunspot drawings is shown.

Over the ages the prevailing view on the nature of sunspots has undergone major revisions. In 1769 the discovery of the Wilson depression changed the prevailing picture of the Sun structure. The Wilson depression refers to the fact that the (visible) radiation from sunspot penumbrae and, in particular, umbrae emerges from a deeper layer than

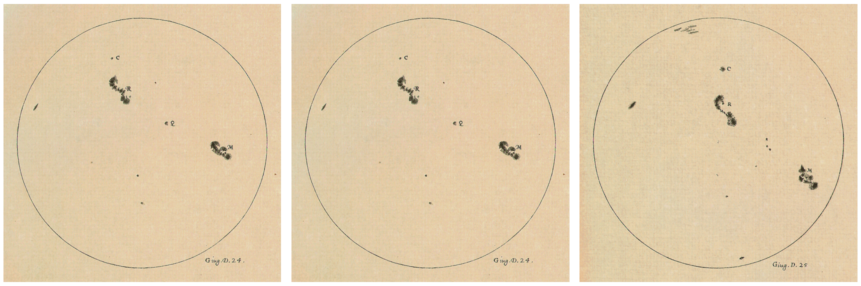

Figure 1.2: Sequence of the Galileo's sunspot drawings.

in the quiet photosphere and it was believed that the entire solar interior was dark and cold (Bray & Loughhead, 1964). The breakthrough in the understanding the nature of sunspots came in 1908, when George Ellery Hale first measured a magnetic field in sunspots (Hale, 1908). Since then the magnetic field has become the root cause of the sunspots phenomenon (Solanki, 2003).

### 1.2.1 Sunspots formation and evolution

Sunspots are the most prominent manifestation of the presence of magnetic fields in the photosphere. Understanding how sunspots form, evolve and decay is a central task to answer open questions concerning the solar dynamo, solar variability and solar magnetohydrodynamics (MHD).

The question of sunspot formation and evolution is investigated using two different approaches. The first approach consists in solar observations using ground and space instruments with high spatial and spectral resolution for spectro-polarimetric data analysis. The second one uses theoretical models to reconstruct the physical processes that occur in sunspots via numerical simulations.

In the tachocline zone shearing motions occur between the fluid motion of the upper-lying convection zone and the stable radiative zone:

these motions contribute to the production of the magnetic fields that, in particular conditions, can emerge in the upper layers of the Sun (Vaquero & Vázquez, 2009). According to the rising-flux tube model (see Parker, 1955), the flux tube forms in the solar toroidal magnetic field and when the magnetic field is sufficiently strong, it becomes buoyant and emerges in the form of flux-tube loops (‘$\Omega - loops$’), mostly oriented in the East-West direction and forming bipolar active regions (AR) (group of sunspots) on the surface. Bipolar active regions show the leading sunspots having all the same polarity in one hemisphere and the opposite polarity in the other hemisphere (Hale’s polarity law). In Figure 1.3 a drawing of the newly formed toroidal magnetic field with the buoyancy of two flux-tubes in different hemispheres is shown.

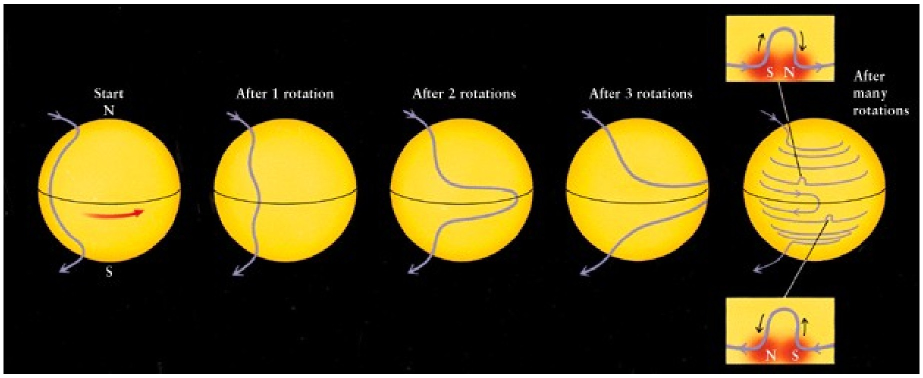

Figure 1.3: Schematic drawing of the solar magnetic field and flux-tube ($\Omega - loops$) formation.

Observations in photosphere show that the magnetic flux emerges mostly at mid and low latitudes. Firstly, the emergence of the magnetic flux causes a disturbance of the solar granulation and the formation of a dark *pore* which grows in time and becomes darker (Loughhead & Bray, 1961). Once the diameter of the pore exceeds roughly 3.5 Mm, it usually starts to exhibit a penumbral structure, whereby the penumbra can be partial (not completely surrounding the proto-spot). The penumbra develops very rapidly, with pieces of penumbra completed within a hour (Bray & Loughhead, 1964; Bumba, 1965; Bumba & Suda, 1984; Leka & Skumanich, 1998; Keppens & Martinez Pillet, 1996; Solanki, 2003). The penumbra grows in bursts, sector after sector, starting with the edge of the sunspot pointing away from the opposite polarity flux of the active region (Zwaan, 1992).

During the formation of an active region, the flux emergence can occur recurrently and leads to the formation of two groups of small magnetic elements of opposite polarity which move outward each other with a speed of about $0.5-1\,\mathrm{km\,s^{-1}}$ (Wang & Zirin, 1992). The process of sunspot formation on the solar surface takes usually from a few hours to several days. As soon as (or even before) the sunspots are completely formed, they begin to decay (McIntosh, 1981; Solanki, 2003).

From a theoretical point of view, there are two main models that try to describe the observed sunspots structure: the monolithic model and the spaghetti-like model. In Figure 1.4 the drawings of the two different models are shown.

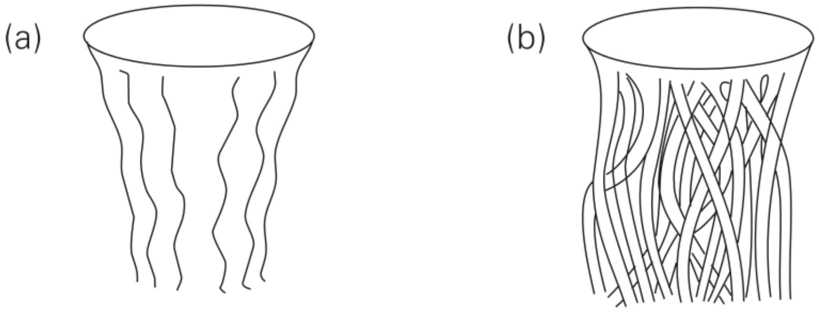

Figure 1.4: Schematic drawing of two magnetic sub-structure models of sunspots. *Left panel (a)*: Monolithic model; *Right panel (b)*: Spaghetti-like model.

The monolithic model is formed by a single vertical magnetic flux tube and there magneto-convective processes occur (Cowling, 1957).

According to the Parker's cluster model (Parker, 1979a,b,c), known as 'spaghetti-like' model, the magnetic flux in the sunspot umbra is concentrated into separate, strongly compressed, vertical magnetic flux tubes that are interspaced with plasma that is almost free of magnetic field; the plasma can move between these tubes.

The spaghetti-like model explains naturally the existence of umbral dots and bright penumbral filaments (see the following sections), but there are two points that must still be clarified: the first one is what forces keep the magnetic field lines together in the photosphere to create long-lived sunspots, the second one is how the magnetic field strength decreases systematically from spot center.

On the other hand, Meyer et al. (1974) studied the possible modes of magneto-convection and predicted the existence of overturning magneto-convective processes for depths larger than 2000 km, in which magnetized and non -magnetized plasma get mixed and the monolithic model is the favourite (Rempel & Schlichenmaier, 2011). Moreover, during recent years different types of theoretical models have been proposed. For a deeper analysis of these models see the review of Solanki (2003).

### 1.2.2 Sunspot properties

The number of sunspots which appear on the Sun strongly varies with time: during the solar activity minimum even no sunspot could appear, while ten or more groups of sunspots are common around the maxima of solar cycles. To study the daily number of sunspots on the Sun, there are two official sunspot numbers in common use.

The first, the daily 'Boulder Sunspot Number', is computed by the NOAA Space Environment Center using a formula devised by Rudolph Wolf in 1848: $R = k(10g + s)$, where R is the Sunspot Number, g is the number of sunspot groups on the solar disk, s is the total number of individual spots in all the groups and k is a variable scaling factor (usually $< 1$) that accounts for observing conditions and the characteristic of telescope.

The second one is the ‘International Sunspot Number’, published daily by the Solar Influences Data Center in Belgium and calculated from the same basic formula of the former. The two methods incorporate data from different observatories (*http : //spaceweather.com/glossary/sunspotnumber.html*).

Sunspots appear in a belt between $+30°$ and $-30°$ from the Sun equator. Moreover, the latitudes of the sunspots vary with the solar activity phase: early in a cycle they appear at high latitudes and in the course of the cycle the new sunspots appear at increasingly lower latitudes. This behaviour was studied by Carrington in 1863 and it is illustrated by the so-called ‘butterfly diagram’ shown in Figure 1.5.

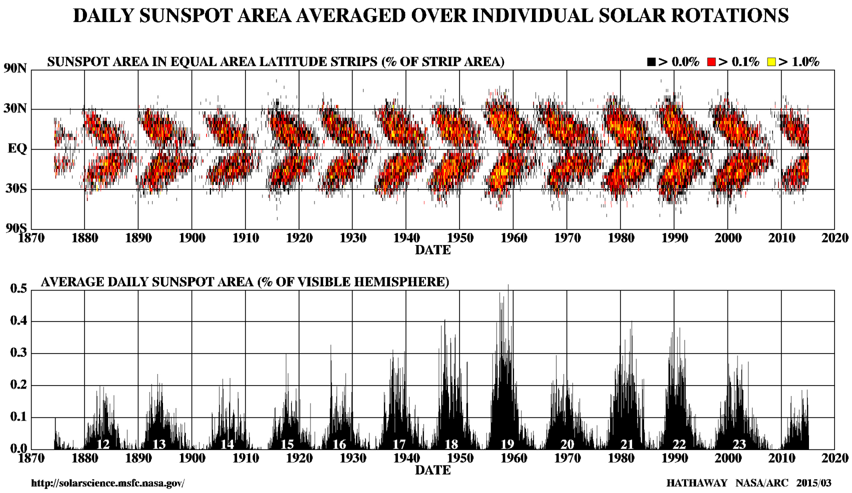

Figure 1.5: Carrington butterfly diagram of sunspots during several solar cycles.

In a sunspot two different parts can be indentified: an inner and darker part, called *umbra*, which radiates roughly $20 - 30\%$ of the wavelength-integrated flux of the quiet Sun, and an outer, less dark part called *penumbra*, which radiates $75 - 85\%$ of the quiet Sun energy flux.

The temperature of the photospheric quiet Sun is 5576 K at $\tau = 2/3$, where $\tau$ represent the continuum optical depth along the line of sight. In the umbra the temperature is 1000 - 1900 K lower than in the quiet Sun, and in the penumbra is 250 - 400 K lower. The temperature is thought to be lowered by the inhibition of the convective energy through the magnetic field. In Figure 1.6 an image of a large sunspot group is shown. In the image the size of the Earth compared with the size of the sunspot is also shown.

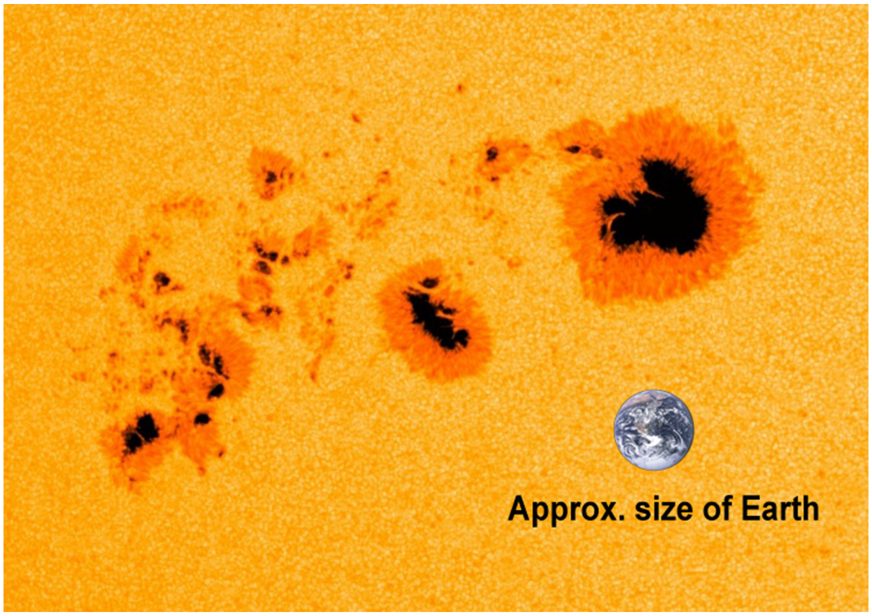

Figure 1.6: Image of one of the largest sunspots observed in the last ten years, labeled AR 1944. Image courtesy of NASA's Solar Dynamics Observatory.

In sunspots the magnetic field gradually varies from the center of the umbra to the edges of the penumbra. In the darker part of the umbra the magnetic field is approximately 2000 - 3700 G and the inclination is close to vertical with respect to the solar surface. At the outer edge of the penumbra the magnetic field is about 700 - 1000 G and it is inclined by 70° $-$ 80° to the vertical. In Figure 1.7 a schematic drawing of the magnetic field inclination in umbra and penumbra regions is shown.

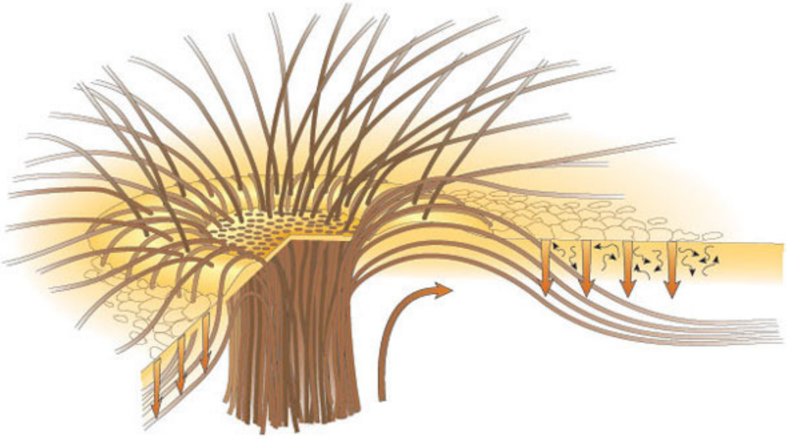

Figure 1.7: Sketch showing the interlocking-comb structure of the magnetic field in the filamentary penumbra of a sunspot. Image from Thomas et al. (2002).

Sunspots exhibit a broad size distribution, even if smaller sunspots are more common than larger ones. Very large sunspots reach diameters of 60000 km or more, while the smallest sunspots can reach diameters of 3500 km (Bray & Loughhead, 1964; Solanki, 2003). The lifetimes of sunspots can be between hours and months, and lifetimes of a day or those longer than a week are now observed thanks to the satellite telescopes. In Table 2.1 the principal parameters of umbra and penumbra are shown.

| **Parameters** | **Umbra** | **Penumbra** |
|---|---|---|
| Brightness | 20 – 30% of quiet Sun | 75 – 85% of quiet Sun |
| Temperature | 3700 - 4500 K | 5000 - 5300 K |
| Magnetic field intesity | 2000 - 3700 G | 700 - 1000 G |
| Magnetic field inclination | vertical | 70° – 80° to the vertical |

Table 1.1: Main parameters of umbra and penumbra of a sunspot.

## 1.3 Small scale structures in sunspots

The comprehension of the physical mechanisms responsible for the formation and evolution of sunspots has been greatly improved thanks to high temporal, spatial and spectral resolution data. These observations have unveiled some physical properties of several fine structures of the sunspots (Thomas & Weiss, 2004) such as: umbral dots (inside the umbra), dark-cored filaments (in the penumbra) and light bridges (LBs, separating some umbral portions). Understanding the interplay between the plasma convection and the magnetic field distribution in sunspot fine structures is fundamental in order to have useful hints on the magnetohydrodynamical processes occurring in the solar atmosphere and in the underlying layers, hidden to the direct observations.

### 1.3.1 Umbral dots

The umbral zone of a sunspot harbors some inhomogeneities which have been called 'umbral dots' by Danielson (1964). They are observed as bright dot-like spots with typical size of $0\farcs5$ or less, embedded in a more uniform and darker background and seem to be present in all the sunspots, although their intensity varies in a significant way (Rempel & Schlichenmaier, 2011). Umbral dots have been sub-categorized in central (CUDs), which appear mostly close the darkest region of the umbra, and peripheral umbral dots (PUDs) which appear at the umbral/penumbral boundary (Loughhead et al., 1979; Grossmann-Doerth et al., 1986). Figure 1.8 shows an image of an umbra with umbral dots inside.

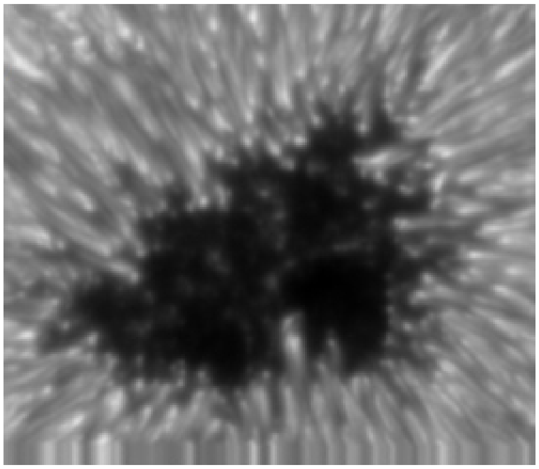

Figure 1.8: Image in the blue continuum of a sunspot taken by SOT/Hinode. The umbral dots are the bright dots in the middle of the dark umbra.

The temperature in the umbral dots at $\tau = 2/3$ is larger than the temperature of the umbral background at the same layer. The temperature difference is between 500 K (Riethmüller et al., 2008) and 1500 K (Socas-Navarro et al., 2004). The temperature difference vanishes at about 200-250 km above $\tau = 1$. Even the magnetic field strength inside the umbral dots is $\tau$-dependent: above the $\tau = 1$ level the difference in magnetic field is small, but fairly large below, where it can be even a few hundred Gauss. Numerical simulations of umbral magneto-convection (Schlusser & Vogler, 2006) predict the existence of upflows at the center of umbral dots and downflows at its edges. Observations confirmed the results of simulations: upflow motions of $0.4 - 1.0\,\mathrm{km\,s^{-1}}$ in the center of umbral dots have been known for quite some time (Rimmele, 2004; Socas-Navarro et al., 2004; Watanabe et al., 2009). In the past few years also downflow motions at the edges of umbral dots have been detected by Bharti et al. (2009) and Ortiz et al. (2010).

### 1.3.2 Light Bridges

Light bridges (LBs) are bright and elongated structures delineating the border between dark umbral cores. In some cases they form during the coalescence process of sunspots, while in other cases they are the evidence of the re-establishment of the granular motions within the spot, and often indicate the beginning of the spot fragmentation (Vazquez, 1973). Moreover, before the formation of a LB, several umbral dots emerge along the area where a LB will be formed, and the LB structure rapidly intrudes from the leading edge of penumbral filaments into the umbra.

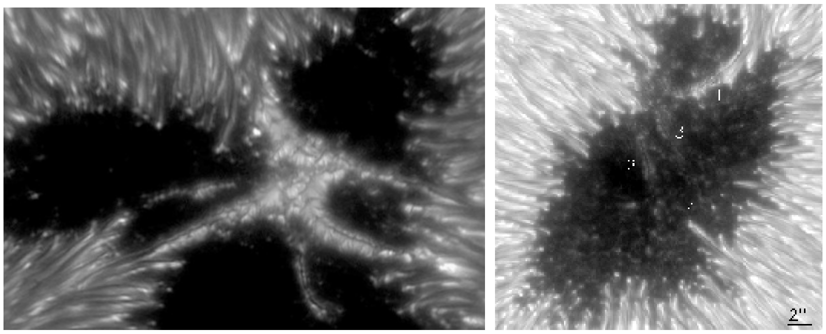

Figure 1.9: *Left panel*: image of segmented light bridges composed by tiny granules; *right panel*: image of an unsegmented light bridge in its formation phase.

Often, a long narrow dark lane runs along an elevated ridge along the length of LBs, and they are segmented by short dark lanes running across them. Basically, a LB is a fissure separating two different parts of a spot and the dark lane is produced by an enhancement of density raising the $\tau = 1$ surface (Priest, 2014). According to Thomas & Weiss (2004) there are two types of LBs: the ones segmented along their length, with bright segments resembling tiny granules separated by narrow dark lanes oriented perpendicular to the axis of the LB (Berger & Berdyugina, 2003), and other, unsegmented, which resemble the elongated bright filaments seen in the penumbra (Lites et al., 2004).

In Figure 1.9 two images of sunspots with LBs are shown. In the *left panel* segmented LBs are shown and in the *right panel* an unsegmented LB almost divides the umbra in two parts. Moreover, LBs are classified as faint light bridges (FLBs, Sobotka & Puschmann, 2009; Sobotka et al., 1993; Lites et al., 1991), which are narrow bright streamers inside the umbra, and as strong light bridges (SLBs, Sobotka et al., 1994), separating different umbral fragments. The FLBs are elongated structures composed by granules of similar size and structure like umbral dots, while the GLBs show granules similar to the quiet Sun. Sobotka & Puschmann (2009) found similar values for the lifetime, size and horizontal velocities in umbral dots and in the granules of a FLB. The mean lifetime of the granules of FLBs is beetween 3.5 and 5.7 min and the average size is about $0\farcs17$.

The intensity of the LB granules is about 0.85 $I_c$ (where $I_c$ is the mean continuum intensity) of the mean photospheric intensity. Following the temporal evolution of these sub-structures during their irregular motions inside the LB, proper motions with velocities up to $1.5\,\mathrm{km\,s^{-1}}$ have been detected (Hirzberger et al., 2002). The lifetime distribution of these granular features shows a maximum at 5 min and a second peak at approximately 20 min (Hirzberger et al., 2002). The Doppler velocity in LB granules shows central upflows surrounded by downflows. According to Louis et al. (2009) and Bharti et al. (2013) the downflows can show supersonic speeds. Lagg et al. (2014) found downflow velocities which reach values of $10\,\mathrm{km\,s^{-1}}$ at the boundaries of GLB granules.

In LBs the magnetic fields have a lower field strength and are sparser and more horizontal than in the neighboring umbrae. LBs with their weak and inclined fields therefore represent a discontinuity in the regular umbral field (Lites et al., 1991; Leka, 1997). However, recent observations by Jurcák et al. (2005) and Jurcák et al. (2006) pointed out an essentially field-free region at the deepest visible level of two LBs, but with magnetic canopies spreading out from either sides of the LBs and merging above them.

Many segmented LBs also show a narrow dark lane along their main axis (Rimmele, 2008). This lane has a typical width that varies from 0.″2 to less than 0.″5 (Berger & Berdyugina, 2003): in the larger section the features (granules along its side) resemble large-scale modified convection, while in the smaller sections of the LB, the granules appear increasingly smaller, until when only a central dark lane is observed, probably due to the alignment of convection cells caused by the magnetic field. Often during the evolution, portions of the dark lane dissolve and then reform again (Rimmele, 2008).

An analysis of a LB velocity field carried out by Rimmele (1997) provided evidence of the presence of sinking plasma in the axial channel. From the correlation between vertical velocity and continuum intensity in the granules belonging to a LB, Rimmele (1997) could confirm their convective origin. In this regard, it would be important to find out whether the motions observed in LBs have a magneto-convective origin or they are due to convection penetrating from the sub-photospheric layers into a field-free gap (Thomas & Weiss, 2004).

More recent observations show that in the granular LBs the dark lane is characterized by upflows, instead of the intergranular lanes of normal granulation where we can see downflows (Rouppe van der Voort et al., 2010). Therefore, the process which originates the dark lane seems to be due to plasma piling up due to a strong decrease of the vertical upflow near the surface. The plasma is forced by the cusp-like surrounding magnetic field in a region with enhanced density and therefore larger opacity (Giordano et al., 2008). This causes the elevation of $\tau = 1$ surface and a cooler, higher part of the atmosphere resulting in the dark lane in intensity images (Schlusser & Vogler, 2006).

Moreover, recent observations have also revealed that some types of LBs are accompanied by remarkable long-lasting plasma ejections or surge activities in the chromosphere (Asai et al., 2001; Shimizu, 2011; Louis et al., 2014).

### 1.3.3 Penumbra structure and filaments

A well developed sunspot typically consists of the dark central umbra surrounded by a less dark annular region called penumbra. The most prominent structures in the penumbra are the radial filaments which are often separated into bright and dark structures (Solanki, 2003). In Figure 1.10 an image of the penumbral filaments is shown.

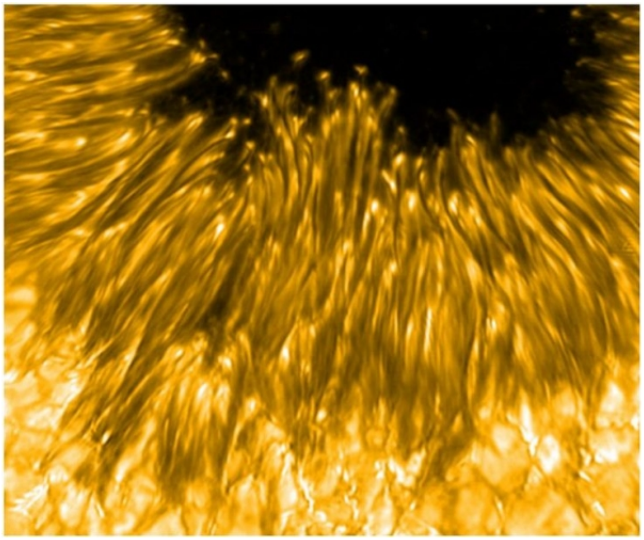

Figure 1.10: Image of a sunspot showing the dark, central umbra (top) with all around the penumbral filaments.

According to Leka & Skumanich (1998), the pore forms the penumbra in sectors when the total magnetic flux reaches $1 - 1.5\ \times 10^{20}$ Mx. Moreover, the penumbra formation is a sudden event, generally within 20-30 minutes and because of this it is difficult to catch observationally, expecially with high spatial resolution observations. The penumbra starts its formation on the side opposite the following polarity of the active region while on the side toward the opposite polarity, the filaments form and disappear because this region is very active and dynamic due to the ongoing flux emergence (Schlichenmaier et al., 2010).

From observations, Sobotka et al. (1999) found that bright penumbral filaments are approximately $0\farcs3$ - $0\farcs6$ broad and $0\farcs5$ - $2\farcs0$ long, but according to Scharmer et al. (2002) most penumbral filaments have a width of $0\farcs2$ - $0\farcs25$. The dark filaments indicate a continuum intensity of $\sim 0.3 - 0.7\, I_c$, while the bright filaments indicate a continuum intensity of $\sim 0.7 - 1.0\, I_c$ (Muller, 1973), with a temperature of 5650 K for the dark fibrils and 100 K hotter than the quiet Sun for the bright fibrils (Suetterlin & Wiehr, 1998). The penumbral magnetic field consists of two major components: spines, where the magnetic field is stronger and more vertical, and intraspines where the magnetic field is weaker and more horizontal (Borrero & Ichimoto, 2011). Such structure of the magnetic field is referred to as ‘interlocking comb’ structure (Thomas & Weiss, 1992) or ‘uncombed penumbra’ (Solanki & Montavon, 1993).

# Chapter 2

# Instruments for solar observations

In this work I used two spectro-polarimetric datasets taken by ground-based telescopes, the Swedish 1-m Solar Telescope and the Richard B. Dunn Solar Telescope, during two coordinated observing campaigns. Data acquired by the Hinode satellite were also analyzed. In this chapter I describe in detail the instruments and their characteristics.

## 2.1 The Swedish 1-m Solar Telescope

The Swedish 1-m Solar Telescope (SST, Scharmer et al., 2003) is located within the Observatorio del Roque de los Muchachos of the Instituto de Astrofísica de Canarias on the island of La Palma, Spain, and is operated by the Institute for Solar Physics of the Royal Swedish Academy of Sciences. The website of SST telescope and the mounted instruments is: $http://dubshen.astro.su.se$. The SST replaced the 50-cm Swedish Vacuum Solar Tower (SVST, Scharmer et al., 1985) by installing a 1-meter telescope on the existing tower and by re-using some of the design and instrumentation developed for the SVST. In Figure 2.1 a picture of the SST telescope is shown.

Figure 2.1: Picture of the Swedish 1-m Solar Telescope in La Palma.

High-quality solar observations require sites with low levels of local and high-altitude turbulence. Sites on high mountains located on rather small islands have proven to be one of the best sites. The SST is located at 2360 m above sea level, but the turbulence near the telescope aperture causes global motion and blurring in the images. Another problem is the scattering from aerosols which can produce a diffuse component that lowers the contrast. When there is strong wind from the Saharian desert an elevated (1000 - 5500 m) layer of mineral dust and dry air reach the Canarian Islands. During this atmosferic event, called *calima*, the seeing conditions could be so bad that observations could be impossible. In addition to the atmospheric effects, solar telescopes suffer from heating by sunlight of the optics and the air within the telescope tube, producing blurred images. To avoid this problem, solar telescopes are either vacuum telescopes, filled with helium, or use careful control of the optic's temperature to reduce heating of the air in the telescope.

### 2.1.1 Telescope description

The SST is a vacuum telescope. Instead of a flat vacuum window, it uses lens to seal off the vacuum. In Figure 2.2 a schematic drawing of the tower with the turret and vacuum system is shown.

The primary optical system is located in the turret on the top of the tower and consists of a lens with a diameter of 1.098 m (clear aperture of 0.97 m) made of fused silica and two 1.4 m flat Zerodul mirrors. Fused silica in the lens were used for their low coefficient of the thermal expansions, which gives small stresses from temperature gradients. Moreover, in order to minimize temperature gradients in the singlet objective, it is mounted on a short cylindrical cell which acts as cooling flange, such that the edges of the lens are exposed to air and with a shield to prevent the cell being heated by direct sunlight. The singlet objective has a center thickness of 82.4 mm. It has a focal length of 20.3 m at a wavelength of 460 nm, is corrected for coma and has a small aspherical correction applied to its first surface

As shown in Figure 2.2, via the two 45 deg turret alt-az mirrors, the beam is directed down through the vertical telescope tube to a primary focus on the bottom plate. The lens itself is a singlet and therefore has enormous chromatic aberrations, i.e., different colors are focused at different distances from the lens. The chromatic aberrations are corrected by a Schupmann system which uses a 60 mm field mirror to deflect the beam upwards and away from the optical axis of the telescope. This beam is mantained within the vacuum system because it is long 5.3 meters, and because the one meter singlet objective is re-imaged on a 25 cm large corrector. This corrector consists of a negative lens and a mirror. The effect of the lens, when used in double pass, is to cancel out the 1-meter fused silica lens, and the effect of the mirrors

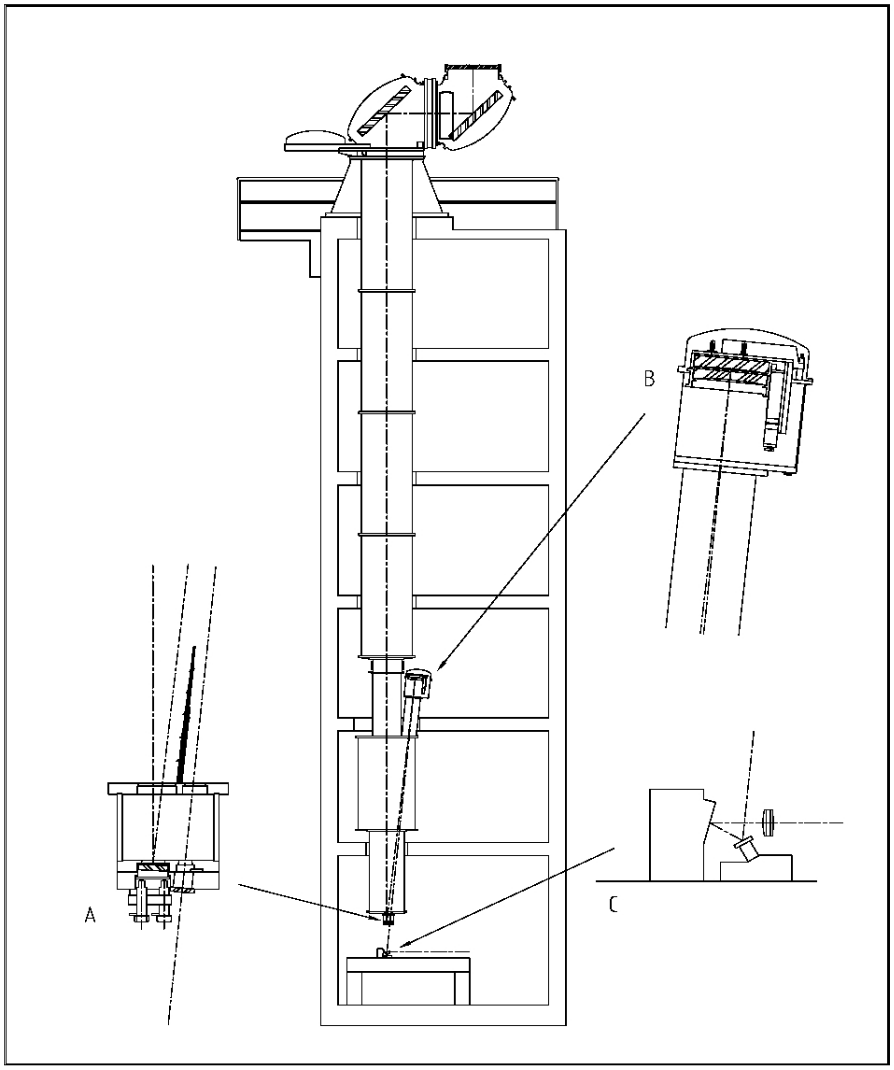

Figure 2.2: Schematic drawing of the SST tower with the turret and vacuum system. *Insert A*: details of the box holding the field mirror and field lens. *Insert B*: the Schupman corrector with one lens and one mirror. *Insert C*: the re-imaging optics, located on the optical table and consisting of a tip-tilt mirror, an adaptive mirror and a re-imaging lens.

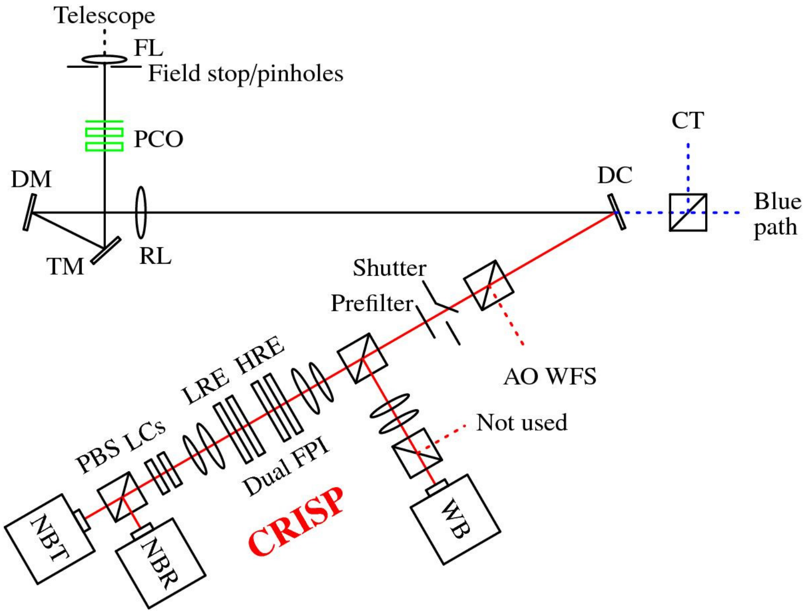

Figure 2.3: Schematic view of the optical setup and the Dual Fabry-Perot

is to create a perfectly achromatic image at the secondary focus.

The following step of the sunlight beam is the Adaptive Optics (AO). In the top part of Figure 2.3 a schematic view of the optical setup below the telescope is shown. Near the focus from the Schupmann corrector there is a field lens (FL) which is designed to form a 34 mm diameter pupil image at the Adaptive Optics deformable mirror (DM).

For monitoring the seeing profile above the telescope, a part of the beam is reflected toward a wide-field wavefront sensor and the other part of the beam pass through the adaptive optics. The AO is composed by the correlation tracker (CT) which measures image motions and uses the tip-tilt mirror (TM) to keep the image steady. Between the target slider and the TM, can be inserted in the beam different polarization calibration optics (PCO) which are not in the beam during normal science observations. The 85-microlens Shack-Hartmann WFS measures the phase of the wavefront at the pupil and tries to keep it flat by controlling the shape of the 85-electrode monomorph DM from CILAS at the rate of 2 kHz. The TM and DM together make the beam horizontal and send it to the reimaging lens (RL). The beam (at 500 nm) is splitted by a dichroic beamsplitter (DC) into a red and blue beams. In the next paragraph is descripted the CRisp Imaging Spectropolarimeter, where only the red beam pass through (see the bottom part of Figure 2.3).

### 2.1.2 CRisp Imaging Spectropolarimeter

The CRisp Imaging Spectropolarimeter (CRISP, Scharmer et al., 2008) is an imaging spectropolarimeter built for the SST. CRISP is based on a dual Fabry-Perot interferometer (FPI) consisting of two etalons mounted in tandem in a telecentric configuration. The FPI is composed by a high spectral resolution etalon (HRE) that defines the observed wavelength and a lower spectral resolution etalon (LRE) that suppresses the first few orders of secondary HRE transmission peaks.The result are quasi-monochromatic images. Moreover, a prefilter limits the spectral range of the light that passes through the optical system, attenuating all higher order transmission peaks of both etalons. Currently ten prefilters are available to observe selected spectral lines and as shown in the bottom part of Figure 2.3 the red beam pass through a prefilter and then a splitter sends the light to the wide-band (8%) and narrow-band channels (92%) respectively. Before and after the etalons, reimaging optics are placed to make the beam slower and to place the focus between the two etalons. To enable polarimetric measurements with low levels of seeing-induced cross-talk from Stokes I to Q, U and V, there are two cameras at the CRISP final focal plane, with the light divided between the two cameras by a polarizing beam splitter. Polarization modulation is made with two tunable liquid crystals (LC's) with two axes at 0° and 45° with respect to the vertical axis on the optical table. The LC's have sufficient stroke to allow full Stokes measurements over the entire wavelength range of CRISP (from about 510 nm to 860 nm). The spectral resolution of CRISP is modest, about 4.4 pm at 538 nm and 6 pm at 630 nm, in order to allow fast tuning of spectral lines at high signal-to-noise level and without spectral undersampling.

## 2.2 The Richard B. Dunn Solar Telescope

The Richard B. Dunn Solar Telescope (DST) is located in the National Solar Observatory at Sacramento Peak, New Mexico. In Figure 2.4 a picture of the telescope tower is shown. It was inaugurated as the world's premier high spatial resolution optical solar telescope in 1969 by the US Air Force as Vacuum Tower Telescope. On September 30, 1998, the telescope was renamed with the actual name in honour of Richard B. Dunn. The website of DST telescope and the mounted instruments is: *http : //nsosp.nso.edu/dst*.

Figure 2.4: Picture of the Richard B. Dunn Solar Telescope in Sacramento Peak.

By removing the air from the telescope and by introducing other innovative concepts in its design, Dunn overcame many hurdles which limited solar telescope performance up to that moment. While larger telescopes have since been developed, the Dunn continues to be the most versatile, user-friendly setup in the world.

DST's structure is like a large iceberg and only a part of its total bulk is actually visible. Approximately 67 meters of this telescope lie out of sight, buried beneath the surface of the peak. The tower portion rises 41.5 meters above ground level and the whole building from top to bottom is a single instrument. In Figure 2.5 a schematic view of the DST structure is shown.

The DST telescope is composed basically by three mirrors, two windows and an evacuated optical path. Sunlight enters the tower through a 76 centimeter window located 41 meters above the ground. The window was placed so high up to avoid distortion of the solar image from local air turbulence near the ground.

As shown in Figure 2.6, a pair of movable 1.1 meter mirrors direct the sunlight down to the 1.2 meter diameter tube that runs vertically down the center of the observing room floor. The sunlight is reflected from the concave 1.6 meter main mirror of the telescope and then back up to the observing room, producing a 51 centimeter diameter image of the sun for detailed studies. The telescope's entire optical system, from the top of the Tower to the base of its underground portion, plus the 12 meter diameter observing room floor, is suspended near the top of the tower by a mercury-float bearing.

The three vertical 1.5 meter diameter tubes clustered around the central tube extending upward through the ceiling contain various optics used for the analysis of sunlight. By slightly tilting the main mirror at the bottom of the central tube with computer control, the sun's image can be focused an any of the spectrographs or at three additional

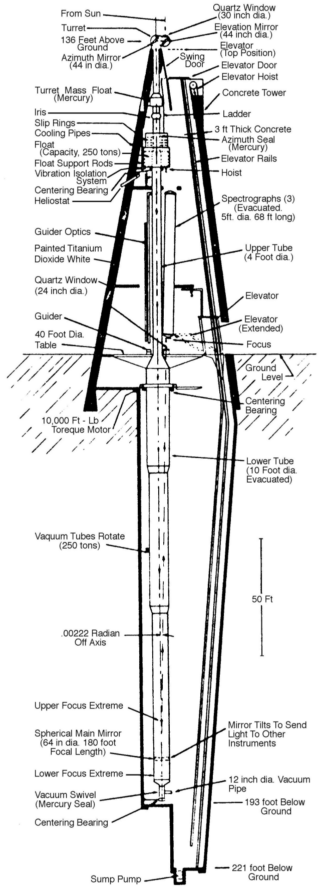

Figure 2.5: Schematic view of the DST telescope.

viewing ports around the central tube.

The DST is equipped with a wide range of excellent instrumentation, such as the Universal Birefringent Filter (UBF), the Advanced Stokes Polarimeter (ASP), the Diffraction-Limited Spectro-Polarimeter (DLSP), the Interferometric BIdimensional Spectropolarimeter (IBIS), Facility Infrared Spectropolarimeter (FIRS) and the Rapid Oscillations in the Solar Atmosphere (ROSA). Moreover, since the late 1990s the National Solar Observatory has been advancing the Shack-Hartmann technique. In 1998 a low-order AO system has been appied to the DST,

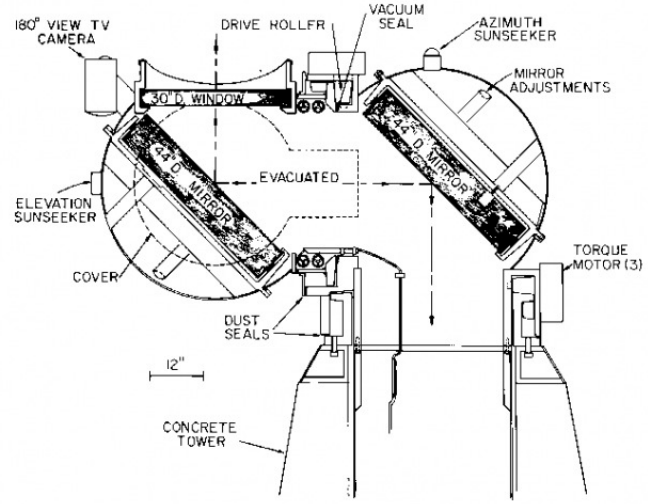

Figure 2.6: Schematic view of the top tower of DST telescope.

thus allowing it to operate near its diffraction limit under moderately good atmospheric conditions. This technology now is applied at several solar telescopes around the world. The current High-Order Adaptive Optics development project is a partnership between NSO and the New Jersey Institute of Technology, supported by the NSF's Major Research Instrumentation division. The DST has also served as the test bed for the ongoing development of the next generation of solar instrumentation.

### 2.2.1 Interferometric BIdimensional Spectropolarimeter

The Interferometric BIdimensional Spectropolarimeter (IBIS, Cavallini & Reardon, 2006) is a high cadence, dual interferometer imaging spectropolarimeter, installed in June 2003 at the DST. IBIS has been built by

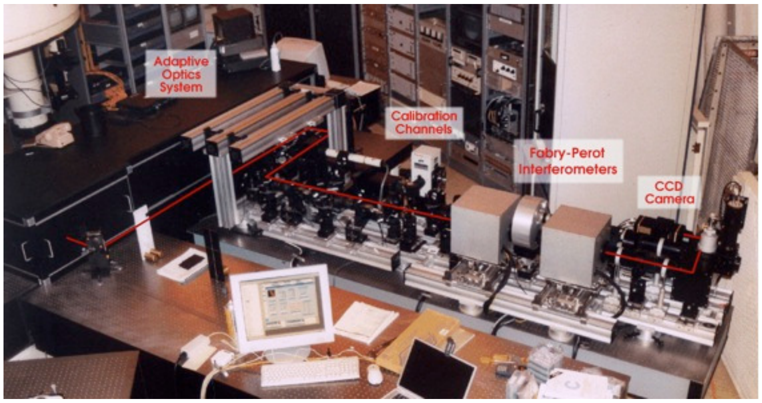

Figure 2.7: The optical layout of IBIS, with the main instrumental components labeled. The primary optical path is indicated in red.

the INAF-Arcetri Astrophysical Observatory, with the support of the Department of Physics and Astronomy of the University of Florence, and the Department of Physics of the University of Rome - Tor Vergata. It is currently operated and supported by INAF in collaboration with the US National Solar Observatory. In Figure 2.7 a picture of the optic table where IBIS is mounted is shown.

In Figure 2.8 a schematic rappresentation of the IBIS layout is shown and the principal optical path is indicated by the solid line. At the exit of the high-order AO, the telescope primary image is at infinity and a pupil image is formed near the first folding mirror m1, at the focus of the transfer lens L0. Then, a solar image of 21.3 mm (corresponding to 80″ on the Sun) is formed on the field stop (FS) by lens L0 and the two mirrors (m2, m3). Three lenses (L1, L2 and L3) and a folding mirror (M1) successively collimate the solar and the pupil image. After the lens L3, the beam pass through the two Fabry-Perot Interferometers (FPIs) used in an axial-mode and in classic mount. Between the two FPIs there are a filter wheel (FWH) carrying a hole, a dark slide and five interference filters. Thanks to a fourth lens L4 and

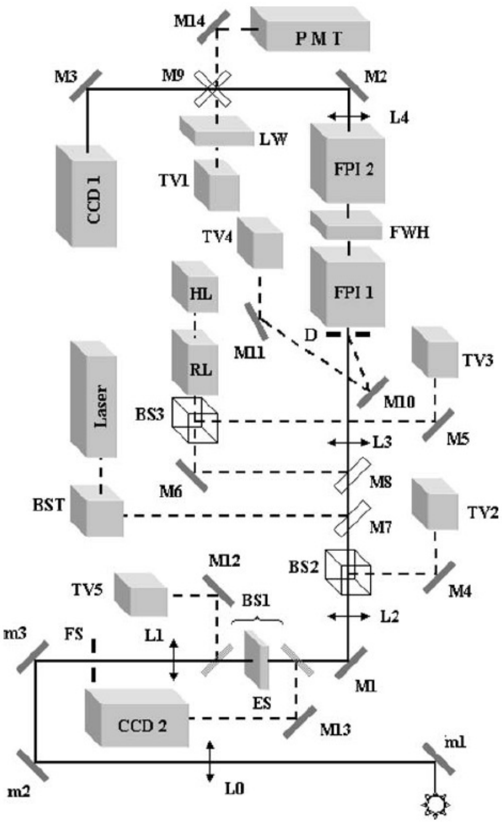

Figure 2.8: Schematic drawing of the IBIS instrumental layout. Solid line: principal optical path. Dotted lines: secondary paths

two folding mirrors (M2, M3), a solar image of 6.85 mm in diameter is formed on a CCD camera (CCD1).

In Figure 2.8 other paths are indicated with dotted lines. For example, there is a *reference path* which create a solar image on the TV5 and CCD2. These images on TV5 are used to show the selected region and to monitor the solar and atmospheric condition. Indeed, CCD2 allows one to take broad-band image of the same FOV, simultaneously with CCD1, which can be used as a transparency reference or for post facto procedures, to correct the seeing effects. Another dotted path is the *tuning path* which is used to find the coincidence of one interference order of FPI 1 with one of FPI2. The last dotted path is the *laser path* which is used to verify and to adjust the parallelism of the interferometer plates.

By means of precise piezo-electric tuning, IBIS can rapidly and reliably scan selected spectral lines within the 580-860 nm range. Thanks to its optical characteristics and to the efficient DST AO system, IBIS produces high-fidelity imaging spectroscopy and polarimetry of the solar photosphere and chromosphere. In Table 2.1 the primary instrumental characteristics are shown.

| | |
|---|---|
| Wavelength range | 5800 Å- 8600 Å |
| Peak wavelengths of the avaible interference filters | 5896 Å(FWHM: 3 Å)<br>6302 Å(FWHM: 3 Å)<br>7090 Å(FWHM: 3 Å)<br>7224 Å(FWHM: 3 Å)<br>8542 Å(FWHM: 5 Å) |
| Spectral resolving power | 190000 - 300000 |
| Wavelength drift | $\leq$ 10 ms$^{-1}$ on 10 h |
| Field of view (circular) | 80” |
| Wavelength setting time | $\simeq$ 20 ms |
| Minimum wavelength step | 4.5 mÅ- 6.6 mÅ |
| Monochromatic camera | Roper PentaMAX 1317x1035 square pixels 6.8 $\mu$m in size.<br>Dyn. range: 12 bits<br>Data rate: 5 MHz |
| Broad band camera | Dalsa CA-D7-1024T 1024x1024 square pixels 12 $\mu$m in size.<br>Dyn. range: 12 bits<br>Data rate: 10 MHz |
| Image scale | $0\overset{\prime\prime}{.}08$ pixel$^{-1}$<br>(2.4 - 3.6 pixels/r.e.) |
| Exposure time (S/N = 100 in the solar continuum) | 27 -50 ms |
| Acquisition rate including: wavelength setting, exposure, frame reading, storing | $\simeq$ 2.5 frames s$^{-1}$ (1024x1024 pixels);<br>$\simeq$ 4 frames s$^{-1}$ (binning 2x2) |

Table 2.1: Description of IBIS characteristics

## 2.3 Hinode Satellite

Hinode, formerly Solar-B, (Kosugi et al., 2007) is a solar satellite mission and the japanese meaning is 'Sunrise'. Hinode was developed, launched, and operated by the Institute of Space and Astronautical Science (ISAS), a division of the Japanese Aerospace Exploration Agency (JAXA), in collaboration with space agency partners from the National Astronomical Observatory of Japan (NAOJ), the United Kingdom, and the United States. The Hinode satellite and the mounted instruments website is: $http://hinode.msfc.nasa.gov/$.

The Hinode spacecraft was launched from Uchinoura Space Center (Japan) on 22 September 2006, at 21:36 GMT, aboard the seventh in JAXA's series of M-V rockets. First light images were captured on 28 October 2006. In Figure 2.9 a picture of the Hinode satellite is shown.

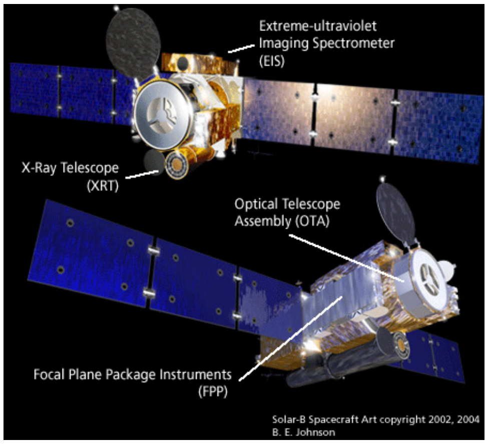

Figure 2.9: Picture of the Hinode satellite.

The principal scientific goals of the Hinode mission are the following (Kosugi et al., 2007):

- understand the processes of magnetic field generation and trasport including the magnetic modulation of the Sun's luminosity;

- investigate the processes responsible for energy transfer from the photosphere to the corona and for the heating and structuring of the chromosphere and the corona;
- determine the mechanisms responsible for eruptive phenomena, such as flares and coronal mass ejections, and understand these phenomena in the context of the space weather of the Sun-Earth System.

Hinode mission includes a suite of three science instruments: the Solar Optical Telescope, X-ray Telescope and Extreme Ultraviolet Imaging Spectrometer. These instruments are important to study the generation, transport, and dissipation of magnetic energy from the photosphere to the corona and record how energy stored in the sun's magnetic field is released, either gradually or violently, as the field rises into the sun's outer atmosphere. In particular, the EUV Imaging Spectrometer (EIS, Culhane et al., 2007) is an imaging spectrometer designed to observe plasmas between the upper transition region and the lower corona. The focal length is 1.9 m, the mirror diameter is 15 cm and the total length of the instrument is 3 m, with an angular resolution of the optics of $2''$. The X-Ray Telescope (XRT, Golub et al., 2007) is a high resolution grazing incidence telescope of a Wolter I design made from Zerodur. The mirror has a 30-cm aperture and a 2.7-m focal length. The XRT consists of the X-ray and visible light optics, focal plane mechanisms (filters and shutter), and the 2k × 2k CCD camera. The optical systems form X-ray and visible light images on a common CCD.

### 2.3.1 Solar Optical Telescope

The study of the response of the chromosphere and corona to changes in the photospheric magnetic field is possible with quantitative measurements of all the three components of the vector magnetic fields. Taking into account that the components of the magnetic field are difficult to resolve from the ground, the Solar Optical Telescope (SOT, Tsuneta, 2008) has been developed to make these observations from the space. The SOT is the largest solar optical telescope flown in the space and consists of the main 50 cm Optical Telescope Assembly (OTA, Suematsu et al., 2007) and focal plane package (FPP, Tarbell et al., 2007). SOT obtains a continuous, seeing-free series of diffraction-limited images ($0\overset{\prime\prime}{.}2$ - $0\overset{\prime\prime}{.}3$) in 388-668 nm range. In Figure 2.10 a scheme of the SOT instrument is shown.

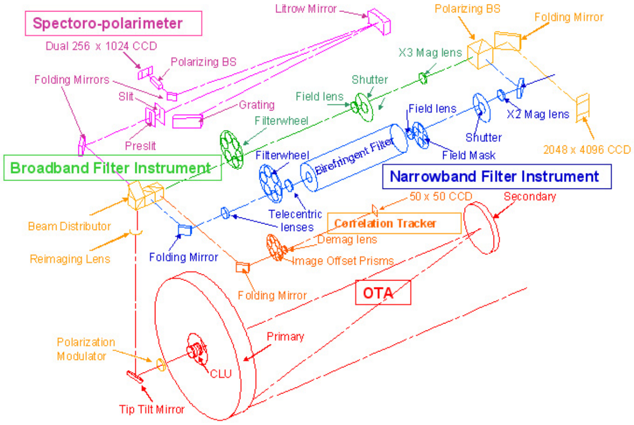

Figure 2.10: Schematic drawing of the SOT instrument.

The distance between the primary and secondary mirrors is 1.5 meters. A heat dump mirror at the primary focus removes the unused solar light (heat) outside of the 328 × 164 arcsecond field-of-view (FOV). The collimator lens (CLU) feeds a collimated light to the FPP. The polarization modulator (PM: a rotating waveplate) is located near exit pupil. All optical elements prior to the PM are rotationally symmetric about the optical axis (except for the secondary mirror supports) in order to minimize instrumental polarization. The folding tip-tilt mirror thus follows the PM. The FPP has four optical paths: the Narrowband Filter Imager (NFI), the Broadband Filter Imager (BFI), the Spectro Polarimeter (SP), and the Correlation Tracker. As shown in Figure 2.10 the BFI and the NFI share a CCD detector and form the Filtergraph (FG). The SP and the CT have their own CCD detectors.

In Table 2.2 properties of the Solar Optical Telescope are shown.

| | |
|---|---|
| *Optical Telescope Assembly (OTA)* | |
| Optics | Aplanatic Gregorian with aperture of 50 cm |
| *Focal Plane Package (FPP)* | |
| Wavelength and lines | **Broadband Filter Instrument (BFI):** |
| | CN (3883.0), Ca II H (3968.5),<br>CH (4305.0), Blue (4504.5),<br>Green (5550.5), Red (6684.0) |
| | **Narrowband Filter Instrument (NFI):** |
| | Mg Ib (5172.7),<br>Fe I (5250.2, 5247.1, 5250.6),<br>Fe I (5576.1), Na I (5895.9),<br>Fe I (6302.5, 6301.5),<br>H I (6562.8) |
| | **Spectro Polarimeter (SP):** |
| | Fe I (6302.5, 6301.5) |
| Sensitivity to magnetic fields | longitudinal : 1 - 5 G<br>transverse: 30 - 50 G |
| Typical time cadence | Ranges from tens of seconds for photospheric images and vector magnetographs in particular lines to ~ 1 hr for the full Stokes profiles |

Table 2.2: Properties of the Solar Optical Telescope

## 2.4 Solar Dynamics Observatory

The NASA's Solar Dynamics Observatory (SDO, Pesnell et al., 2012) was launched the 11th of February 2010 at 10:23:00 a.m. aboard of the United Launch Alliance Atlas V rocket from Launch Complex 41 at Cape Canaveral Air Force Station. The SDO satellite and the mounted instruments website is:$http : //sdo.gsfc.nasa.gov/$. In Figure 2.11 a picture of the SDO is shown.

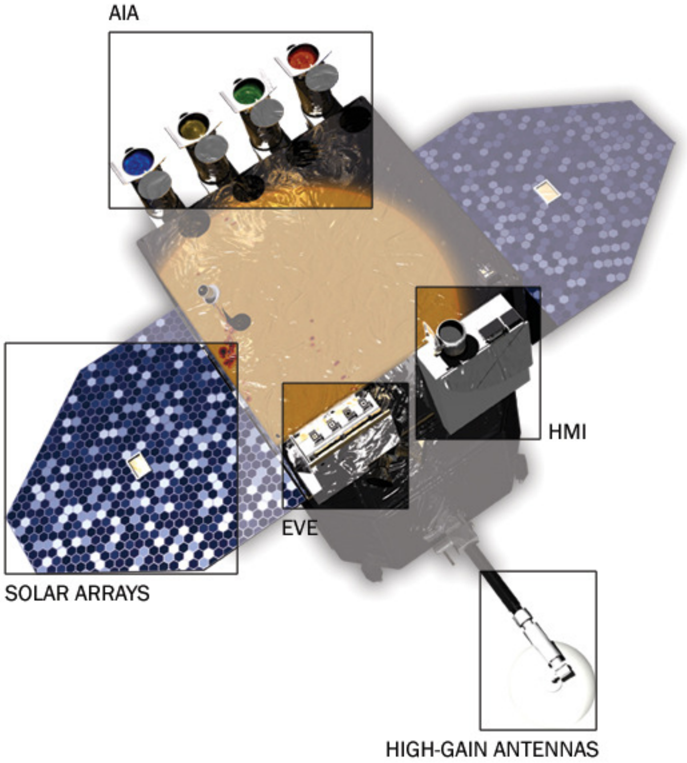

Figure 2.11: Picture of the Solar Dynamics Observatory.

The scientific goals of the SDO Project are to improve our understanding about:

- what mechanisms drive the quasi-periodic 11-year cycle of solar activity;
- how active region magnetic flux is synthesized, concentrated, and dispersed across the solar surface;
- how the large-scale field topology and current systems are reorganized by the magnetic reconnection on small scales and how it is significant in heating the corona and accelerating the solar wind;
- which configurations of magnetic field lead to the CMEs, filament eruptions, and flares that produce energetic particles and radiation;
- the possibility of make accurate and reliable forecasts of space weather and climate.

SDO contains a suite of instruments that provide observations leading to a more complete understanding of the solar dynamics. The three instruments on board SDO are the following:

1) The Helioseismic and Magnetic Imager (HMI, Scherrer et al., 2012), designed to study oscillations and the magnetic field at the solar surface. HMI observes the full solar disk at 6173 Å with a resolution of $1''$and is a successor to the Michelson Doppler Imager (MDI) on the Solar and Heliospheric Observatory (SOHO).
2) The Atmospheric Imaging Assembly (AIA, Lemen et al., 2012) is designed to study the solar corona, taking simultaneous full disc images in multiple wavelengths of the corona and transition region (up to half a solar radius above the solar limb), with 1.5 arcsec resolution and 12 second temporal cadence or better. The primary goal of the AIA science investigation is to significantly

improve our understanding of the physics behind the activity displayed by the Sun's atmosphere, which drives space weather in the heliosphere and in planetary environments. In Table 2.3 the wavelenghts observed by AIA are shown.

| **Channel** | **Primary ion(s)** | **Region of atmosphere** | **log(T)** |
|---|---|---|---|
| 4500 Å | continuum | photosphere | 3.7 |
| 1700 Å | continuum | temperature minimum,<br>photosphere | 3.7 |
| 304 Å | He II | chromosphere,<br>transition region | 4.7 |
| 1600 Å | C IV + cont. | transition region,<br>upper photosphere | 5.0 |
| 171 Å | Fe IX | quiet corona,<br>upper transition region | 5.8 |
| 193 Å | Fe XII, XXIV | corona and hot flare plasma | 6.2, 7.3 |
| 211 Å | Fe XIV | active-region corona | 6.3 |
| 335 Å | Fe XVI | active-region corona | 6.4 |
| 94 Å | Fe XVIII | flaring corona | 6.8 |
| 131 Å | Fe VIII, XXI | transition region,<br>flaring corona | 5.6, 7.0 |

Table 2.3: The primary ions observed by AIA.

3) The Extreme Ultraviolet Variability Experiment (EVE, Woods et al., 2010) measures the solar EUV irradiance with unprecedented spectral resolution, temporal cadence, and precision. EVE measures the solar EUV spectral irradiance to understand variations on the timescales which influence Earth's climate and near-Earth space.

# Chapter 3

# Evolution of the magnetic field inclination in a forming penumbra

In this chapter we describe the evolution of the magnetic and velocity fields in the annular zone around a pore a few hours before the formation of its penumbra. We present the results obtained by analyzing data acquired during the observing campaign at the DST, Sunspot (New Mexico), from the $23^{th}$ to $31^{th}$ May 2012. The following data analysis allows us to describe the variations of the plasma velocities along the line of sight (LOS) and of the intensity, azimuth, and inclination angle of the magnetic field a few hours before the formation of the penumbra. The results of this analysis suggest that the penumbra formation originated from changes in the inclination of the field lines in the magnetic canopy overlying the pore, until they reach the photosphere (Romano et al., 2014).

## 3.1 Observations and data analysis

The AR NOAA 11490 was observed on the $28^{th}$ May 2012. We used both continuum filtergrams and LOS magnetograms taken by the HMI on SDO in the Fe I line at 617.3 nm with a resolution of 1″in order to study the global evolution of the active region.

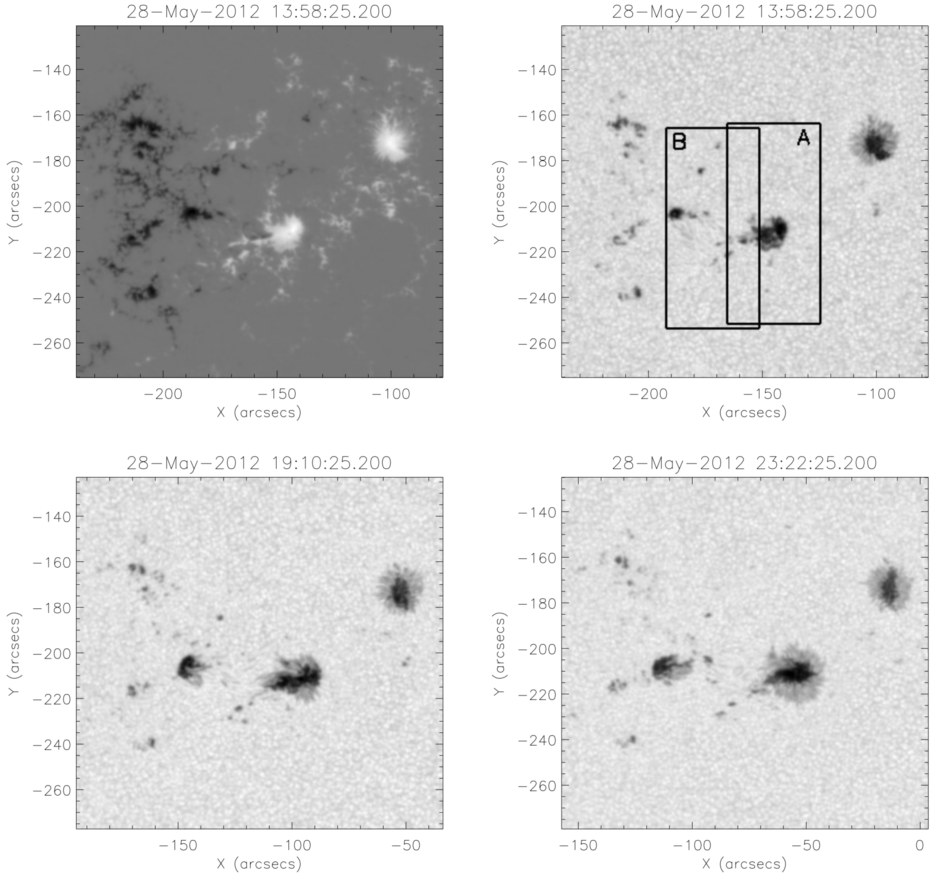

Figure 3.1: AR NOAA 11490 as seen in the LOS magnetogram (*top left panel*) and its evolution in continuum filtergrams taken by HMI/SDO at 617.3 nm. The boxes A and B in the *top right panel* indicate the FOVs observed by IBIS.

Figure 3.1 (*top left panel*) shows the magnetic configuration of the whole AR on the $28^{th}$ May 2012 at 13:10 UT. The region consists of two preceding main sunspots with positive polarity and a more diffuse negative polarity in the following part of the AR. As can be seen in the sequence of continuum filtergrams shown in Figure 3.1 (*top right* and *bottom panels*), the southern part of the AR was characterized by a rapid evolution phase. In particular, the southern positive polarity corresponds to a pore at 13:58 UT ( Figure 3.1, *top right panel*), which showed the complete formation of its penumbra in about 10 hr, from about 13:00 UT to 23:00 UT (*bottom right panel*).

In this work we analyzed observations of the AR NOAA 11490 ($\mu \sim 0.95$) acquired on the $28^{th}$ May 2012, from 13:39 UT to 14:12 UT, by the Interferometric BIdimensional Spectrometer operating at the DST. In particular, the results presented therein are derived from analysis of the observations of the field of view A indicated in Figure 3.1.

This FOV is characterized by the presence of a pore, which developed a penumbra. The data set essentially consists of 30 scans of the Fe I 630.25 nm line, observed in spectropolarimetric mode, and of the Ca II 854.2 nm line, observed without polarimetric measurements. The Fe I and Ca II lines have been sampled with a FWHM = 2 pm and an average step = 2 pm, corresponding to 30 and 25 wavelength points, respectively. The pixel scale in the data of both lines was $0\farcs09$, while the integration time per wavelength was 60 ms. To deduce the evolution of the intrinsic magnetic field strength, inclination and azimuth angles, and the LOS velocity in the photosphere, we performed a single-component inversion of the Stokes profiles of all the available scans of the Fe I 630.25 nm line using the SIR code (Ruiz Cobo & del Toro Iniesta, 1992). The physical parameters LOS velocity, field strength, and inclination and azimuth angles are assumed to be constant with height. We modeled the stray-light contamination by averaging over all Stokes I spectra in the 64 pixel characterized by lowest polarization degree. We used the spectral point-spread function of IBIS (Reardon & Cavallini, 2008) to take into account the finite spectral resolution of the instrument. We neglected the correction of the result for the Local

Solar Frame because the position of the target is very close to the disk center.

We also estimated the LOS velocity of the plasma in the chromosphere from the analysis of the Ca II line scans. Since there is no absolute wavelength reference in IBIS observations, we considered the median of the Ca II line centroid in the whole FOV as wavelength reference. Then we estimated the plasma velocity from the Doppler shift of the centroid of the line profile in each spatial point with respect to this median.

## 3.2 Results

During the whole observation time interval of IBIS observations lasting 32 minutes we detect the presence of an annular zone around the pore of AR NOAA 11490 and the persistence of its main magnetic and dynamics characteristics. In Figure 3.2 we show the continuum intensity, the strength and inclination angle maps of the magnetic fields at the beginning and end of the observational time interval.

In the *top left* and *top right panels* of Figure 3.2 is visible a slight variation of the pore shape, but there are not significant variations of the other two parameters shown in Figure 3.2 (strength and inclination of the magnetic field). Inside the contour of Figure 3.2 the magnetic flux is about $1.1 \times 10^{21}$ Mx during the observation interval and only a slight intensification of the magnetic field strength in the annular zone around the pore is visible when comparing the two middle panels. In the two bottom maps we measured an average inclination of the field in the annular zone of about $60^\circ$. At its external edge, we detected the presence of some regions characterized by an inclination of the magnetic field larger than $135^\circ$ and by a typical size of about $1''$. These regions, characterized by a circular shape, according to their inclina-

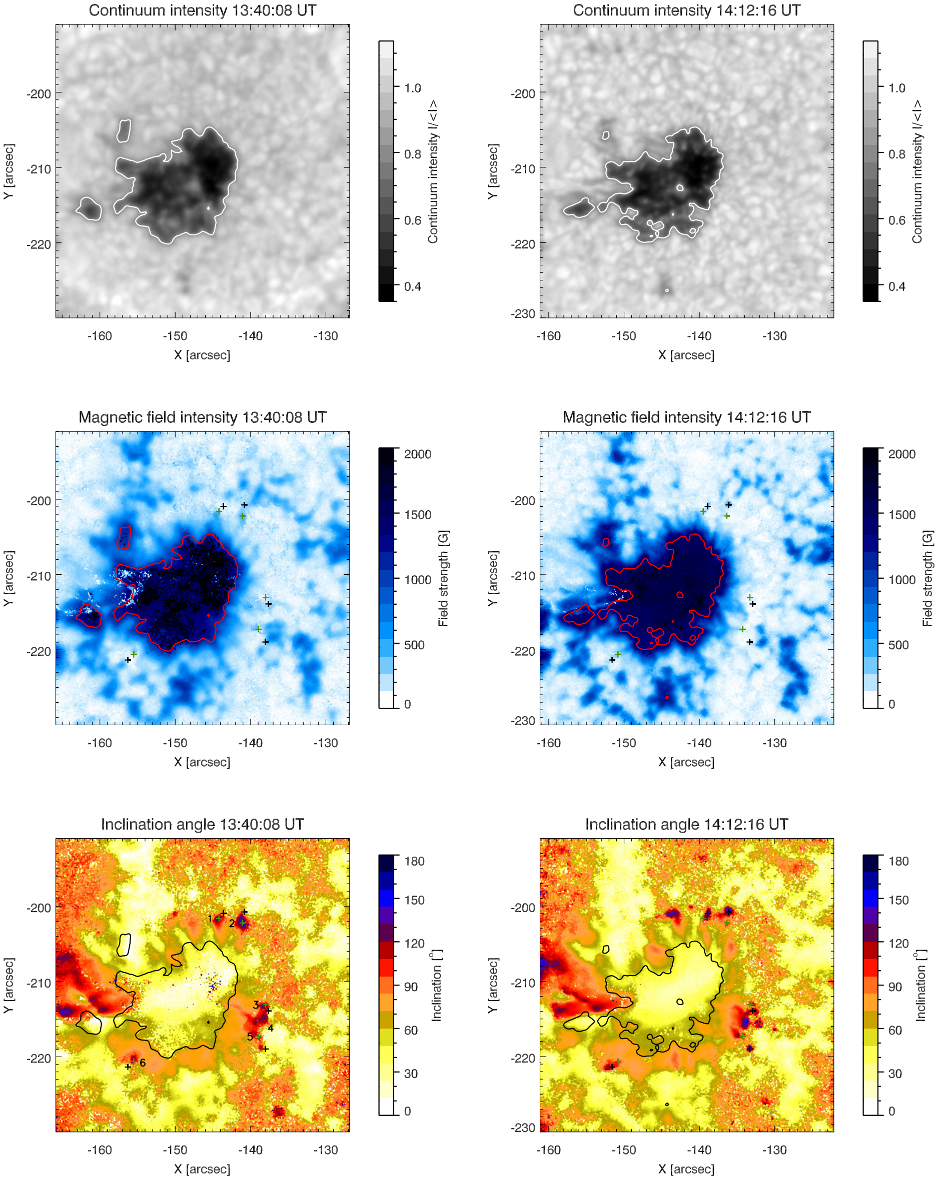

Figure 3.2: Snapshots of the intensity (*top panels*), strength (*middle panels*), and inclination (*bottom panels*) maps of the magnetic fields obtained from the Fe I 630.25 nm line taken by IBIS at the beginning (*left column*) and end (*right column*) of the observation time interval. The green and black crosses indicate the location of the patch barycenters at the beginning and end of the observation time interval, respectively.

tion angle, correspond to regions with a polarity opposite to that of the pore. We analyzed the dynamics and the magnetic field properties of these patches in order to understand their role in the penumbra formation process. We studied in detail the patches visible during the whole observation time interval, numbering them from 1 to 6 in the *bottom left panel* of Figure 3.2. In the *bottom panels* green and black crosses are drawn indicating the position of the patch barycenters at the beginning and end of the observation time interval, respectively. From the comparison of these images we observe that all patches move radially outward covering a distance of $1''$or $2''$. The horizontal velocities of the patches are between 1.0 and 2.0 $\mathrm{km\,s^{-1}}$. In Table 4.1 we summarize the physical parameters of the patches studied over the whole observing time interval: patch 4 was not considered because its evolution was very complex and characterized by merging with other neighboring patches.

| Patch | Average Field Strength (G) | Area ($10^{15}\,\mathrm{cm}^2$) | Magnetic Flux ($10^{18}\,\mathrm{Mx}$) | Inclination (deg) | LOS Velocity (km s−1) |
|---|---|---|---|---|---|
| 1 | 1030 | 1.9 | 2.1 | 140 | 0.7 |
| 2 | 850 | 4.5 | 3.9 | 143 | 0.7 |
| 3 | 420 | 2.1 | 0.9 | 152 | 2.5 |
| 5 | 560 | 1.5 | 0.9 | 145 | 0.5 |
| 6 | 730 | 0.6 | 0.5 | 145 | 1.3 |

Table 3.1: properties of the analyzed patches.

In Figure 3.3 *(top panels)* we show the LOS velocity maps of the plasma obtained from the inversion of the Stokes profiles of the Fe I at 630.25 nm. In these maps is visible an enlargement of the annular zone from $3''$ to $5''$. Moreover, in these maps is visible the lack of upflow plasma in the annular zone and an average downflow of 1.0 $\mathrm{km\,s^{-1}}$. We observe upflow plasma only in the region of the patches all around the annular zone and the upward plasma velocity is between 0.5 and 2.5 $\mathrm{km\,s^{-1}}$.

In Figure 3.3 *(bottom panels)* we show the Doppler velocity maps of the plasma deduced from the time series of Ca II observations.

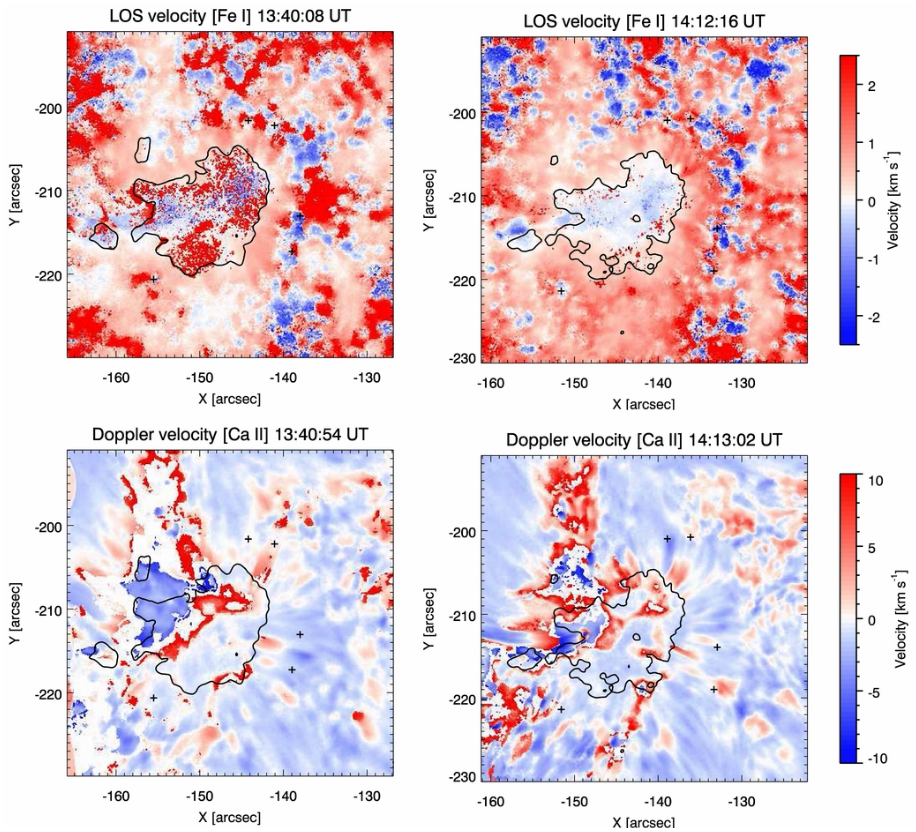

Figure 3.3: Maps of the LOS velocities derived from photospheric observations at the Fe I (*top panel*) and chromospheric observations at the Ca II line (*bottom panels*) at the beginning (13:40 UT) (*left column*) and end (14:12 UT) (*right column*) of the observation time interval. The crosses indicate the location of the patch barycenters. The blue (negative) and red (positive) velocities indicate upflow and downflow, respectively. North is at the top, west is to the right.

These maps show that the patches (except patch number 1 which is going to disappear) are located at the outer edge of the annular zone and mostly in the same direction of the elongated regions characterized by the strongest chromospheric downflow. Observing the Doppler velocity maps is evident that there are not patches in the east side of the pore where there are more elongated regions of chromospheric upflow.

## 3.3 Discussion

The position of most of observed patches, in the north and southwest part of the annular zone, correspond to regions where the penumbra starts to form (see the *bottom left panel* of Figure 3.1) The location of the patches studied and their inclination higher than 135°, suggest that they can be the footpoints of the magnetic field lines starting from the pore and returning to the photosphere. Rempel (2011) found a similar result in his MHD simulation of the fine structure of an already formed penumbra. Noteworthy results concerning our study of the properties of the patches can be summarized as follows:

- the typical size of each patch is of the order of $1''$, with a magnetic flux of the order of $10^{18}$ Mx;
- the outward velocity of each patch is about $1.0\,\mathrm{km\,s^{-1}}$, up to $2.0\,\mathrm{km\,s^{-1}}$;
- the width of the whole annular zone increases from $3''$to $5''$;
- presence in chromosphere of elongated regions of downflow plasma motions.

This evolution of the observed region can be interpreted as a conseguence of the field lines that going down to the photosphere, modify progressively the photospheric plasma motions and develop the penumbra. In Figure 3.4 (top panel) we show a schematic drawing to explain the process where the magnetic field lines of the magnetic canopy overlying the pore change their inclination and reach the photosphere. In this drawing the patch is indicated by the blue oval and the dashed arrow indicates its radial outward displacements. The blue arrow indicates the upflow velocity observed in photosphere in correspondence of the photospheric layer, while the red arrow at the chromospheric layer represents the regions characterized by the strongest downflow velocity observed in the Ca II Doppler maps.

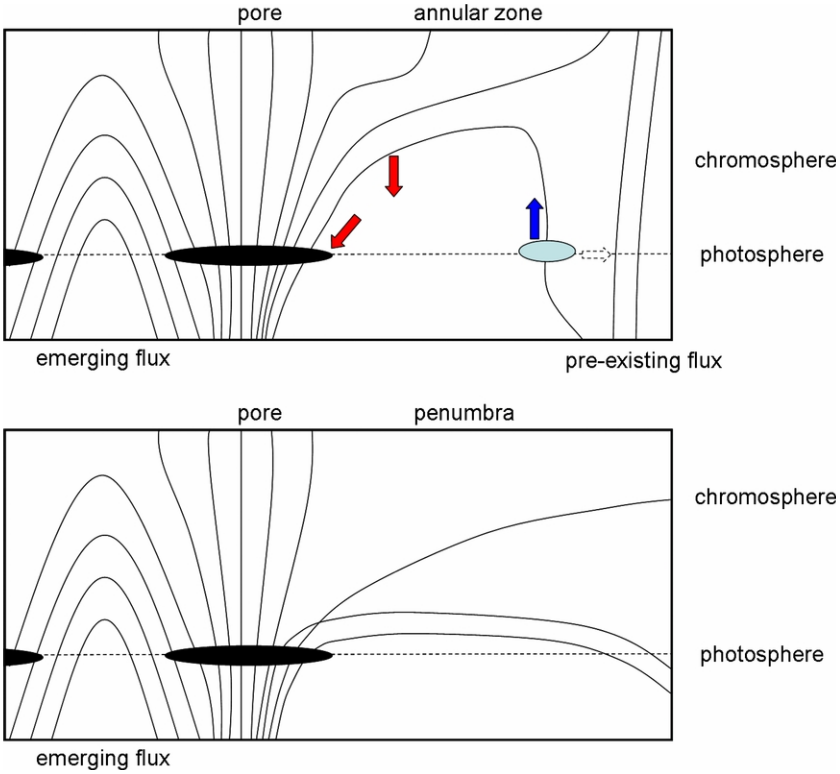

Figure 3.4: Sketch of the magnetic field configuration before (*top panel*) and after (*bottom panel*) the penumbra formation. The colored arrows indicate the prevalent motions observed at the photospheric and chromospheric levels, while the dashed arrow indicates the radially outward displacement of the patches (blue oval).

In Figure 3.4 (bottom panel) the uncombed configuration of the magnetic field after the penumbra formation is represented.

In the above scenario there are two elements that need further investigation: i) in the SDO/AIA images we did not observe any brightenings that could be interpreted as signatures of some reconnection process causing a magnetic reconfiguration and variation of the field line inclination and ii) it is not clear which could be the mechanism that pushes down the magnetic field from the overlying atmospheric layers to the photosphere.

# Chapter 4

# Kinematics and magnetic properties of a light bridge in a decaying sunspot

In this chapter we present the results obtained by analyzing high spatial and spectral resolution data of the solar photosphere and cromosphere acquired during the observing campaign at the SST, La Palma (Spain) from the $6^{th}$ to $19^{th}$ August 2011. The results obtained in this study support and confirm outcomes of recent MHD simulations showing the presence of upflows in LBs.

## 4.1 Observations and data analysis

The AR NOAA 11263 was observed on the $6^{th}$ August 2011, at N16W43 ($\mu = 0.76$), using the CRisp Imaging Spectropolarimeter mounted at the Swedish Solar 1-m Telescope, during a joint observing campaign with the Hinode satellite. The CRISP spectropolarimetric measurements were taken from 09:53:32 UT to 10:48:43 UT along the Fe I line pair at 630.15 nm and 630.25 nm in 15 spectral points for each line, with steps of 4.4 pm from -26.8 pm to 34.8 pm for 630.15 nm and steps of 4.4 pm from -30.8 pm to 30.8 pm for 630.25 nm with respect to the line center of each line. Cristaldi et al. (2014) used the same kind of dataset for a different target observed during this observing campaign. The average cadence of each scan was 28 seconds. Liquid crystals modulated the light cycling through four polarization states, and 5 exposures per polarization state were acquired, resulting in a total of 20 exposures per line position. The pixel size of the CRISP cameras was $0\farcs06$ pixel$^{-1}$ at 630.15 nm and 630.25 nm. The field of view (FOV) of these SST measurements was $57\farcs5 \times 57\farcs3$.

Moreover, the dataset acquired by Hinode satellite during the joint observing campaign was used to obtain information on the magnetic field topology of the AR. The Hinode/SP recorded the Stokes profiles along the Fe I line pair at 630.15 nm and 630.25 nm with a pixel sampling of $0\farcs317$ and a noise level of about $10^{-3} I_c$ (normal mode). Level 2 data obtained from the 'MERLIN' inversion code (Lites et al., 2007) were used in our analysis. We applied to the inverted dataset the nonpotential magnetic field calculation technique (NPFC, Georgoulis, 2005) to perform azimuth disambiguation in solar vector magnetograms, obtaining inclination and azimuth angle maps in the local solar frame.

To follow the global evolution of the AR and the formation of the LB we also analyzed continuum images and LOS magnetograms in the Fe I line at 617.3 nm from $2^{nd}$ to $7^{th}$ August 2011 taken by HMI. Both dataset were characterized by a pixel size of $0\farcs5$ and a time cadence of 2 hours.

The SST data have been processed using the Multi-Object Multi-Frame Blind Deconvolution (MOMFBD, van Noort et al., 2005) technique in order to achieve the highest spatial resolution in combination with the adaptive optics. For the data processing we followed the different steps in the CRISPRED reduction pipeline for CRISP data (de la Cruz Rodríguez et al., 2015). Wide band images, acquired simultaneously with the spectro-polarimetric scans, have been used as a so-called anchor channel in the reduction procedure to ensure precise alignment between the sequentially recorded CRISP narrowband images. Following the data calibration, we obtained two three-dimensional datacubes containing restored, aligned data with a high angular resolution of $0\overset{\prime\prime}{.}16$. The blueshift variation from the center of the FOV towards the edge, due to the Fabry-Pérot system, was corrected during the reduction procedure.

We applied to the SST sequence acquired at 10:17 UT, obtained during the best seeing condition, the SIR inversion code to obtain maps of the magnetic field strength and temperature in a sub-array FOV centered on the LB region. We inverted with the SIR code simultaneously the spectra acquired in both the lines of the Fe I line pair at 630.1/630.2 nm. Stokes I values in the red wing of the Fe I 630.25 nm line were not included in the profile of the inverted pixels because the signal is altered by telluric lines and, for low temperatures, by molecular blends. We used two different models as initialization of the inversion, depending on the region, identified by a threshold in the continuum intensity, forming the FOV: penumbra ($0.4 < I_c < 0.8$) and umbra ($I_c < 0.4$).

In the penumbral model, we changed the temperature (T) and the electron pressure ($p_{e^-}$) using the values described by del Toro Iniesta et al. (1994), and we used a value of 1000 G for the magnetic field strength and of $1.0\,\mathrm{km\,s^{-1}}$ for the LOS velocity. For the umbral model we used the T and $p_{e^-}$ values provided by Collados et al. (1994), (an umbral model for a small spot), and we kept the constant value of 2000 G for the magnetic field strength. The temperature stratification of each component was modified with 2 nodes. The other physical parameters (magnetic field, LOS velocity, inclination and azimuth angles) were assumed to be constant with height (number of nodes equal 1). A fixed macroturbolence of $2.95\,\mathrm{km\,s^{-1}}$ was used in order to mimic the effects of the spectral PSF of the instrument. A fixed filling factor of 1 was used for the inversion. The straylight contamination was not considered during the inversion owing to the fact that the Stokes I profile in the Fe I line at 630.2 nm is heavily affected by blends, thereby severely affecting our hability to determine its contribution. We decided to apply more weight to Q, U, and V Stokes parameters, by a factor of 4 with respect to Stokes I owing to the larger noise in the intensity than in the polarization profiles. The CRISP dataset was not used to study the inclination angle because the LB's FOV was not sufficient to apply the NPFC code.

To study the kinematics in the LB region, we obtained the Doppler velocity of plasma motions by applying a Gaussian fit to the Fe I line profile at 630.15 nm with the MPFIT routine (Markwardt, 2009) in IDL. The LOS velocity map was calibrated by subtracting the mean velocity of the pixels of the umbra in the FOV (pixels which have a threshold of the $I_c$ lower than 0.4).

## 4.2 Results

We can see in Figure 4.1 the HMI/SDO continuum image and the corresponding magnetogram taken on the $3^{th}$ August 2011 relevant to the AR NOAA 11263. At that time, the AR is characterized by a preceding main negative polarity sunspot and by several smaller positive polarity ones (see *left* and *right panels* of Figure 4.1). We note the roughly circular compact structure of the preceding spot and some negative polarity structures of smaller size in the northern and southern part of the following region.

Figure 4.2 shows the evolution of the preceding spot from the $3^{th}$ to the $6^{th}$ August. The well-defined umbra and penumbra (Figure 4.2, *top left panel*), start to fragment on the $4^{th}$ August, when the penumbra filaments in the north-western part of the spot seem to penetrate in

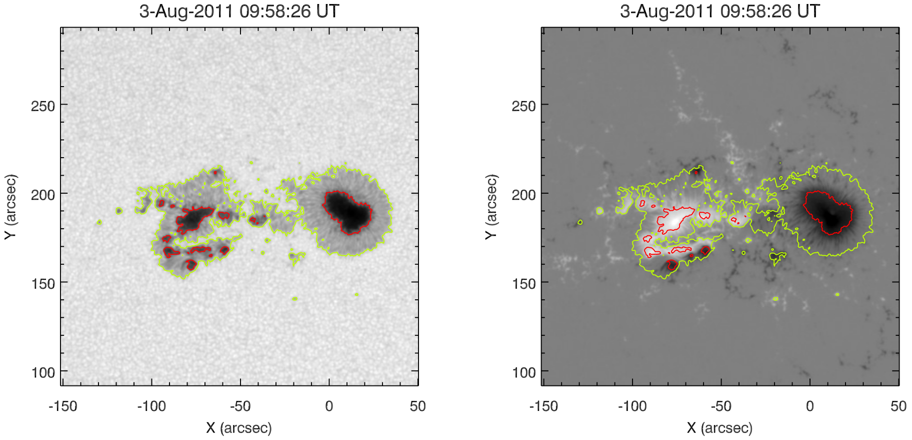

Figure 4.1: Continuum intensity map (*left panel*) and LOS magnetogram (*right panel*) of AR NOAA 11263 obtained by HMI/SDO at the Fe I 617.3 nm line on the $3^{th}$ August 2011. The red and green contours indicate the umbra and penumbra borders, as derived by applying an intensity threshold set to $I_c$=0.5 and $I_c$=0.9 to quiet Sun continuum intensity value, respectively. North is at the top, West is at the right.

the umbral region (see the red contour in Figure 4.2, *top right panel*). On $5^{th}$ August (Figure 4.2, *bottom left panel*) the preceding sunspot exhibits two umbrae with different shapes, one more elongated and the other one with a more circular shape, inside the same penumbra. The LB appears and completes its formation on the $6^{th}$ August, before the start of the CRISP observations analysed in the following (the CRISP's FOV is indicated by the box in Figure 4.2, *right bottom panel*).

Figure 4.3 shows the continuum intensity map observed by CRISP on the $6^{th}$ August at 10:17 UT, with the LB oriented approximately along the north-south direction. It is worth noting that the radial distribution of the penumbral filaments is modified in the regions near the LB. In fact, penumbral filaments south of the LB are smaller than the others around the sunspot. Moreover, in this area the photospheric

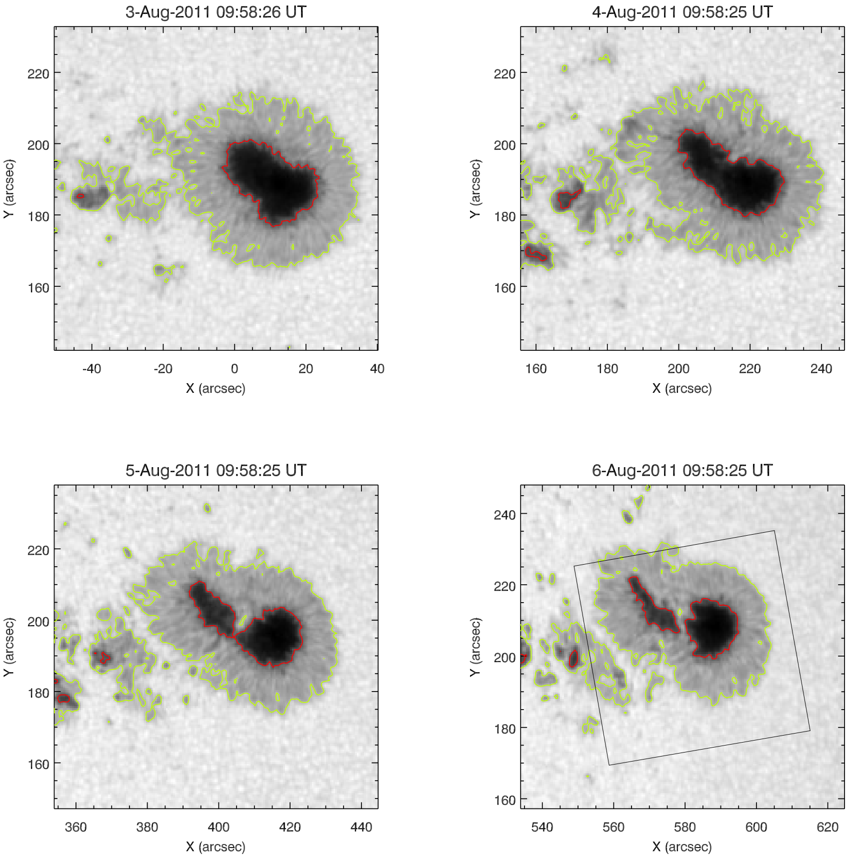

Figure 4.2: HMI/SDO images in the continuum of the Fe I line at 617.3 nm of the preceding sunspot of AR NOAA 11263 taken on consecutive days, from the $3^{th}$ to the $6^{th}$ August 2011. The FOV is $\sim 90 \times 90$ arcsec. The color contours have the same meaning as in Figure 4.1. The sequence shows the evolution of the sunspot umbra and the formation of the LB. The box in the *bottom-right panel* indicates the FOV of the CRISP observations analysed in our study and shown in Figure 4.3.

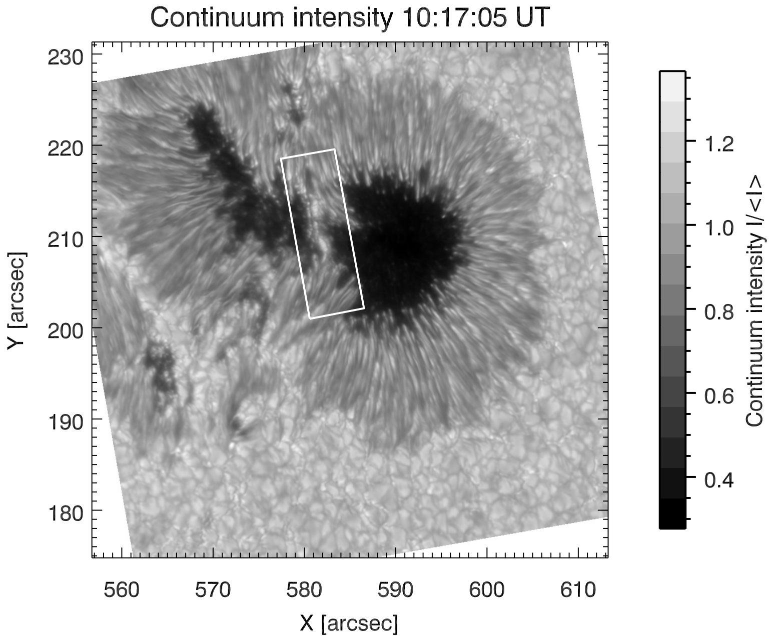

Figure 4.3: Continuum intensity map of the preceding sunspot of AR NOAA 11263 obtained by CRISP in the Fe I 630.15 nm line on the $6^{th}$ August 2011 at 10:17 UT. The solid box indicates the LB's FOV analyzed in the following (see text).

granulation seems to prevail over the penumbra. Further, to the north-east of the LB we note some small dark regions characterized by a local higher value of the magnetic field strength (compare with Figure 4.4, *top panel*).

In Figure 4.4 we show the magnetic field strength and inclination angle maps obtained by the MERLIN inversion on Hinode/SP data. The magnetic field strength map suggests that in the LB region, the upper part has magnetic field strength lower than in the bottom part. The inclination map shows a similar trend: the magnetic field is more inclined in the upper part of the LB. In general, the inclination angle map shows in the region of the LB an inclination angle lower than the vertical direction corresponding to the two umbral zones.

We restricted our analysis of the LB properties to the data acquired by CRISP/SST at 10:17 UT in the FOV indicated by the box reported in Figure 4.3 and Figure 4.4. We divided the LB into two parts, characterized by a different configuration of the magnetic field at its sides: the northern part (corresponding to the upper part of the LB and indicated by $LB_n$ in Figure 4.5 and Figure 4.6) with the larger umbral core of the spot at the eastern side and the penumbral filaments at the opposite side (compare with Figure 4.3), and the southern part (corresponding to the bottom part of the LB and indicated by $LB_s$ in Figure 4.5 and Figure 4.6) with the two umbral cores at both sides.

In Figure 4.5 (*top panel*) we show a $\sim 90^\circ$ rotated zoomed image of the LB region displayed in Figure 4.3 (white box), where the black line indicates the dark lane of the LB. The narrow dark lane along the main axis of the LB has an average width of $0\farcs3$ and a length of about $8\farcs0$. It seems to connect two dark penumbral filaments located at both sides of the LB. Moreover, the LB appears segmented along its length by tiny granules (sizes from $0\farcs2$ to $0\farcs8$) separated by narrow dark lanes oriented perpendicularly to the LB axis.

In Figure 4.5 (*bottom panel*) the LOS velocity along the dark lane is plotted using a pixel unit. This plot shows that, in the $LB_n$ region, the LOS velocity values are between 0 and $-0.2\,\mathrm{km\,s^{-1}}$ (negative velocity values indicate upflows), while, in the $LB_s$ region, the LOS velocity is higher and can reach up to $-0.6\,\mathrm{km\,s^{-1}}$. We therefore note that the dark lane shows mostly upward motions, which appear to be higher in $LB_s$ than in the dark lane of $LB_n$ where upward motion is strongly reduced, but we also notice that here the LB is located between an umbral region and a penumbral one.

Therefore, in order to investigate how the configuration of the magnetic field at the LB sides can influence the dark lane properties, we

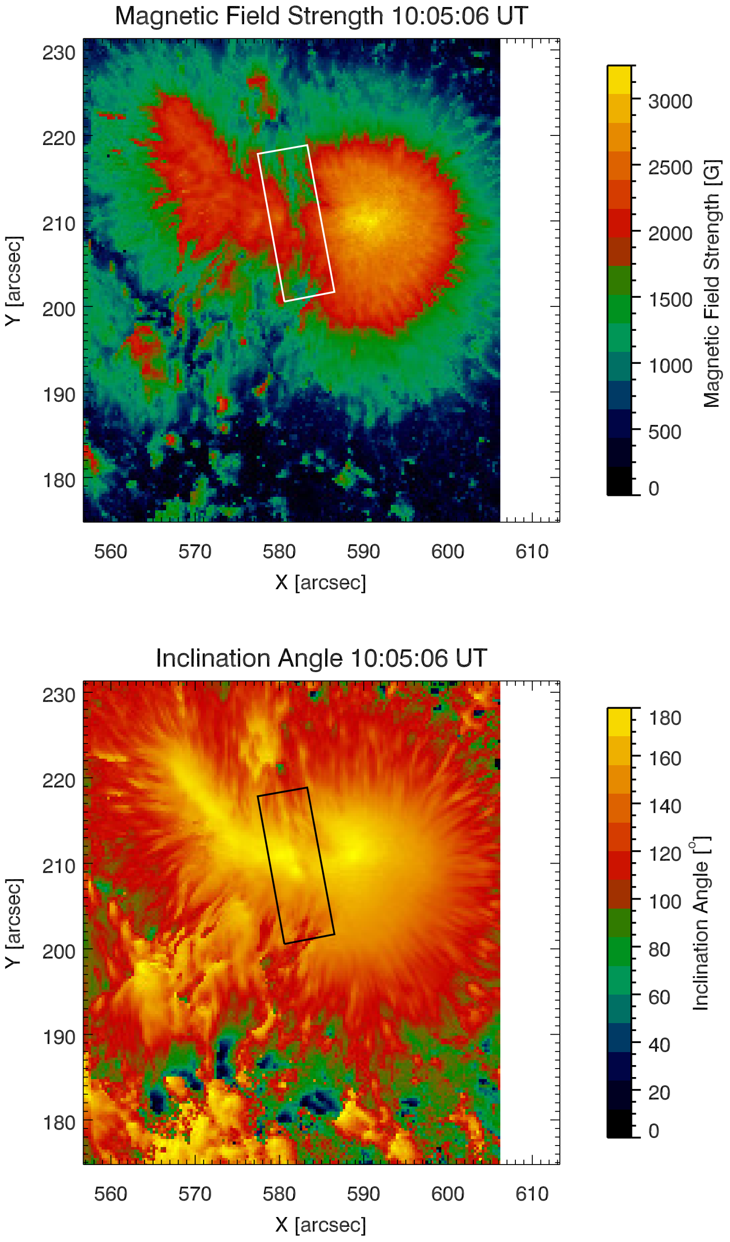

Figure 4.4: Maps of the magnetic field strength and inclination angle obtained from the inversion of both Fe I 630.15 nm and 630.25 nm lines dataset taken by Hinode on the $6^{th}$ August 2011 at 10:05:06 UT. The region with X> 606″ is not covered by Hinode observations. In each map the solid box indicates the LB's FOV analyzed (see text).

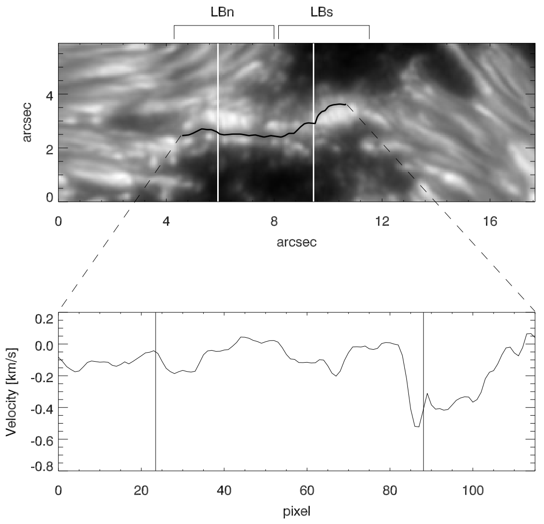

Figure 4.5: Continuum intensity map from CRISP observations of the LB with overplotted a black line indicating the position of the dark lane studied (*top panel*) and LOS plasma velocity values (*bottom panel*) estimated along the dark lane highlighted on the intensity map. The two white lines in the *top panel* and the two black lines in the *bottom panel* correspond to the lines 1 and 2 reported in Figure 4.6.

studied the $I_c$, the magnetic field strength, the temperature, and the LOS velocity inside and around the LB (see Figure 4.6) with particular attention to the vertical segments reported in Figure 4.5 (*bottom panel*), where the LOS velocities of the dark lane are completely different.

The granules at the western side of the $LB_n$ (see the white arrow in the $LB_n$ portion in Figure 4.6, *top left panel*) are larger than the ones at the eastern side (conversely in the southern part of the LB). The maps of the magnetic field strength and of the temperature at $\log(\tau_5) = 0.0$ obtained by the SIR inversion (Figure 4.6, *top right* and *bottom*

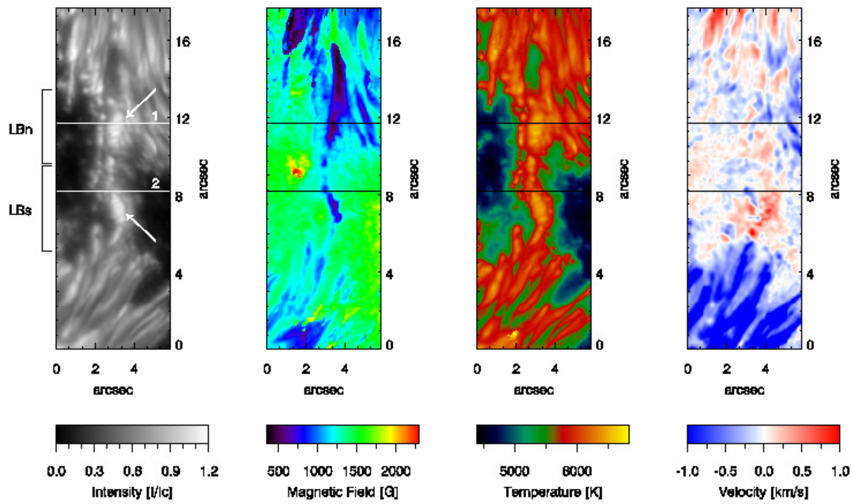

Figure 4.6: From*left to right*: maps of the continuum intensity, magnetic field strength, LOS velocity and temperature of the region containing the LB, at 10:17 UT (CRISP dataset). The maps of the magnetic field strength and temperature have been obtained from the SIR inversion of the Stokes profiles along the Fe I 630.15 nm and 630.25 nm lines. In the velocity map, derived from Doppler measurements, positive (negative) values correspond to downflow (upflow) motions. The white lines in the intensity map and the dark lines in the other maps correspond to the pixels studied in Figure 4.7. In each map, line 1 indicates a region of $LB_n$ and line 2 indicates a region of $LB_s$.

*left panels*) indicate that the granules of the LB that are characterized by a larger size correspond to regions with a weaker magnetic field and a higher temperature. The LOS velocity of the plasma along the LB is on average lower in value (of the order of $\sim \pm 0.6\,\mathrm{km\,s^{-1}}$) than the LOS velocity in the neighbouring penumbral filaments, where the LOS component is of the order of $\sim 2\,\mathrm{km\,s^{-1}}$ due to the Evershed flow (note that in Figure 4.6, *bottom right panel*, the LOS velocity value are saturated to make more visible the LOS velocity values along the LB).

In Figure 4.7 we analyzed the $I_c$, the magnetic field strength, the temperature, and the LOS velocity along the two segments perpendicular to the LB drawn in Figure 4.5 (*bottom panel*) and Figure 4.6. The plots in the *left* and in the *right columns* of Figure 4.7 correspond to the above physical quantities along the segments in the northern and in the southern part of the LB, indicated in Figure 4.6 by labels 1 and 2, respectively. The vertical line in the plots indicates the location of the dark lane.

We note that the intensity of the dark lane is about $0.8\,I_c$ for both parts of the LB (see Figure 4.7, *top panels*). In the $LB_n$ (Figure 4.7, *top left panel*) we see that at both sides of the dark lane there are two maxima in the $I_c$. They correspond to the granules of the $LB_n$ along the line 1. The largest granule has a size of about $0\farcs8$ and is characterized by a magnetic field strength between 700 and 1000 G (see Figure 4.7, *second left panel*). The smallest granule has a size of about $0\farcs2$ and a magnetic field of about 1500 G. The same behavior is detected in the region selected in $LB_s$ (see Figure 4.7, *first two right panels*). The temperature at $\log(\tau_5) = 0$ in the dark lane is about 6000 K (see Figure 4.7, *third panel* from the top), while the larger granules of the $LB_n$ reach a temperature of about 6400 K.

In Figure 4.7 we note that the dark lane in the $LB_n$ is almost at rest (see *bottom left panel*), while the granules at its sides are charac-

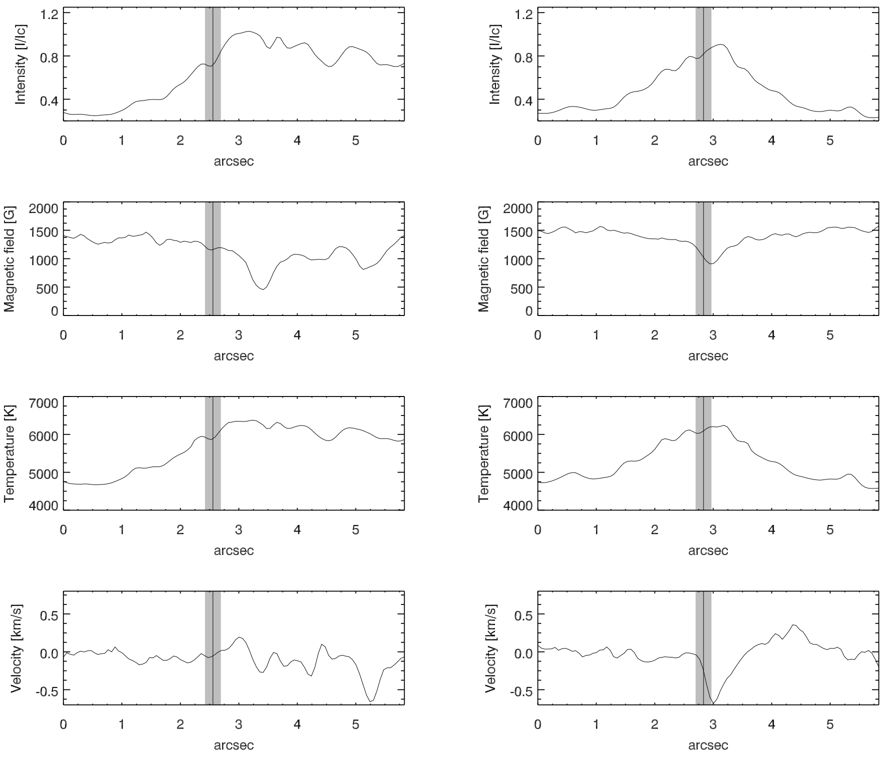

Figure 4.7: *Left column*: from the top to the bottom, plots of $I_c$, magnetic field strength, temperature and velocity along line 1 (see Figure 4.6). *Right column*: the same parameters along line 2 (see Figure 4.6). In these plots the black vertical line shows the dark lane position and the grey line shows its width.

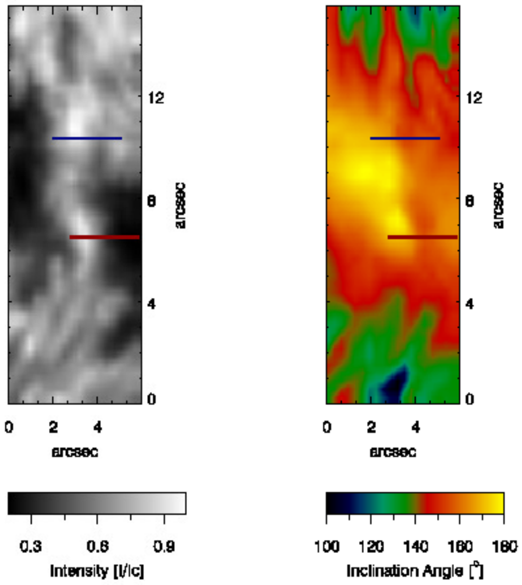

Figure 4.8: Maps of the $I_c$ (*left panel*) and inclination angle (*right panel*) of the region containing the LB (see the solid box in Figure 4.3 indicating the LB FOV analyzed) deduced from Hinode/SP observations at 10:05 UT. The blue and red segments correspond to the white lines 1 and 2, respectively, shown in Figure 4.6 (*left-top panel*).

terized by downflow motions (higher in the larger granule). The dark lane in the $LB_s$ (see *bottom right panel*) shows upflows of the order of $\sim -0.6\,\mathrm{km\,s^{-1}}$ and downflows between 0.1 and $0.4\,\mathrm{km\,s^{-1}}$ in the surrounding region.

In order to study how the inclination angle changes inside and in the surroundings of the LB, we used the data acquired by Hinode/SOT at 10:05 UT. In Figure 4.8 the Hinode maps of the continuum intensity and inclination angle of the region containing the LB are shown.

We studied the profile of the magnetic field inclination along the two segments drawn in Figure 4.6 and reported in blue and red colors in Figure 4.8. The inclination angle along the blue line of Figure 4.9 (which refers to the $LB_n$ region, located between an umbral region and a penumbral region) shows that in the eastern umbral region the magnetic field inclination has values around 170°, it reaches values lower than 155° in the center of the $LB_n$ and slightly more vertical values in the western penumbral region. In the $LB_s$ (red line in Figure 4.9), located between two umbral regions, the inclination angle decreases to a minimum in the $LB_s$ ($\sim 155°$), but at both sides in the umbra the inclination angle is $\geq 165°$.

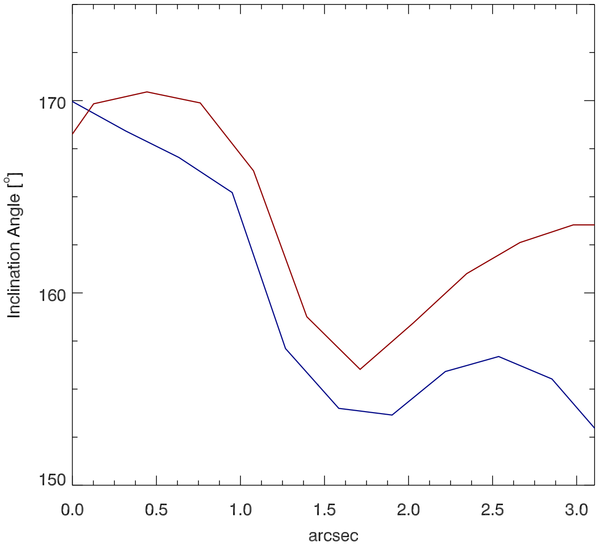

Figure 4.9: Plot of the inclination angle along the blue and red lines of Figure 4.8. The blue curve corresponds to the inclination angle along the $LB_n$ located between an umbral and a penumbral zone. The red curve corresponds to the inclination angle along the $LB_s$ located between two umbral cores.

## 4.3 Discussion

Nordlund & Scharmer (2010) found a cusp-shaped central dark lane in a LB formed in a three-dimensional MHD simulation of field-free gap surrounded by an umbral-like atmosphere and predict that the dark lane in sunspot LBs harbors upflows. The confirmation of these outcomes derived from numerical simulations with observations is challenging. High spatial resolution observations have shown in fact that LBs are highly spatially structured, with convective motions occurring at spatial scales of few tens of arcseconds. The mixing of information from these features, if not resolved, can thus lead to wrong estimates of the sign of the plasma velocities, thus explaining the discrepancy of results reported in the literature (Rimmele, 1997). Moreover, we observed a different behavior in the plasma motions in the $LB_s$ and $LB_n$, characterized by different magnetic field configurations at the surroundings. The $LB_s$ is located between two regions with almost vertical magnetic fields (see in Figure 4.9 the red curve). The dark lane in this region hosts upward motions with LOS velocity between $-0.2$ and $-0.6\,\mathrm{km\,s^{-1}}$, as shown also in Figure 4.5. This last finding is in agreement with the results of Rouppe van der Voort et al. (2010) and confirms the hypothesis that the dark lane is a cusp-like region where the plasma piles up as a consequence of braking of vertical flows.

On the other hand, the $LB_n$ is located between regions with an almost vertical magnetic field at one side and a more inclined one on the other side (see in Figure 4.9 the blue curve). The dark lane in this region shows weaker upward motions, probably indicating that the process of plasma piling up in this condition is somehow modified.

Therefore, we conclude that the configuration of the surrounding magnetic field can play an important role not only in the formation of a cusp-like region with enhanced density and corresponding to the dark lane, but also in the vertical upflow usually observed along these structures. The results obtained from our study thus support recent MHD simulations and observations of magneto-convection in sunspot atmospheres.

# Chapter 5

# Properties of granules in a LB and in the quiet Sun

In this chapter we investigate the properties of the granules in a LB observed in the preceding sunspot of AR NOAA 11263, in order to compare them with a sample of granules observed in the quiet Sun. Continuum intensity data acquired at the SST have been analysed using a new identification algorithm for the solar granulation. Firstly, we describe the algorithm implemented and than we show the obtained results. Different values in size, mean continuum intensity and Doppler velocity in the granules of the LB with respect to those in the quiet Sun have been found and discussed.

## 5.1 Algorithm description

A new automatic technique able to identify granules has been developed. As shown in Figure 5.1, granules correspond to peaks in the intensity image. This information has been exploited in the design of the proposed solution. Specifically, the algorithm consists of the following steps:

- Gaussian filtering;

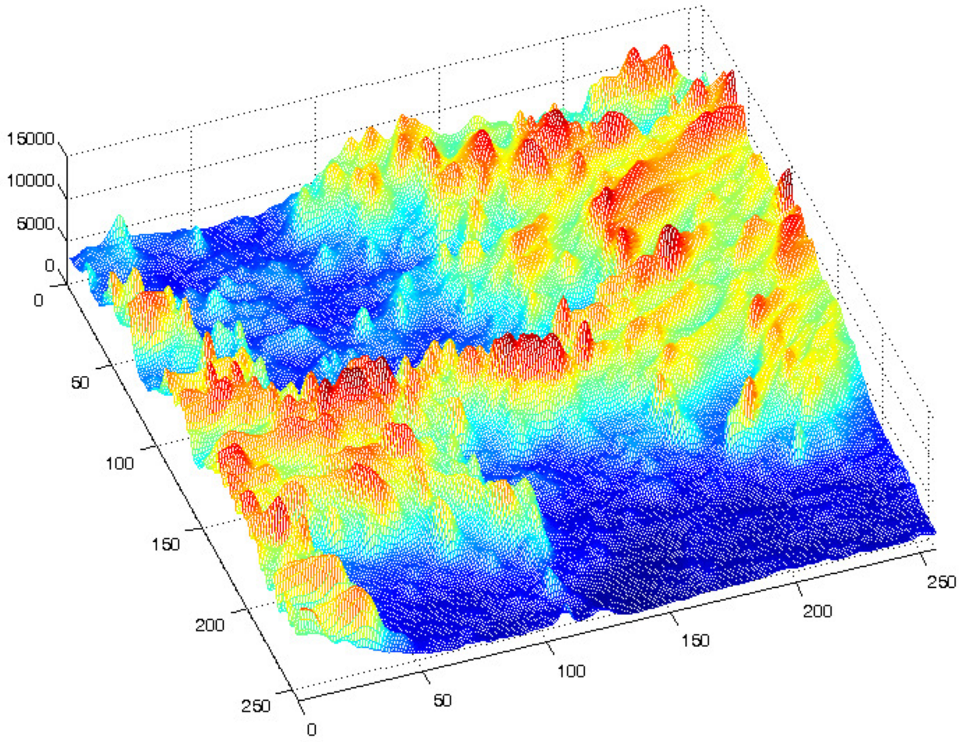

Figure 5.1: 3D intensity image. Granules are clearly visible as peaks.

- local maxima computation;
- image segmentation;
- region refinement based on slope analysis;
- region refinement based on intensity histogram.

To reduce the noise in the original image and remove less important local maxima, a Gaussian filtering is first applied. Once the image has been filtered, the proposed solution finds local maxima. The image is then partitioned into $N$ regions (one for each local maximum). This segmentation is performed dividing the intensity image into $M$ sets.

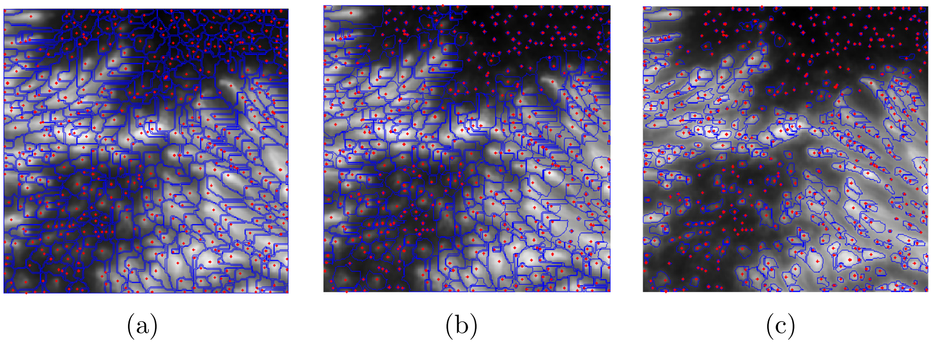
(a) (b) (c)

Figure 5.2: Examples of several steps of the proposed solution: (a) overall image segmentation based on the local maxima previously located (in red); (b) first refinement based on slope analysis; (c) final labeling.

Specifically, these sets of points are built from the intensity image $I$ as follows:

$$S_k = \{(i,j) | T_h * (k-1) \leq I(i,j) < T_h * k\} \quad k = 1, \ldots, M \tag{5.1}$$

where $T_h = max(I)/M$.

Starting from the highest to the lowest set (i.e., from $S_M$ to $S_1$), unlabeled pixels are assigned to the nearest regions. In particular, at the generic iteration $k$, for each pixel $p \in S_k$, the Euclidean distance with respect to all the already assigned pixels at the previous iteration (i.e., $k-1$) is exploited to perform the assignment task. It is worth noting that at the first iteration, the only pixels already assigned to the $N$ regions are the local maxima previously located.

As can be noted from Figure 5.2(a), the performed segmentation partitions the overall image into disjoint regions that can be used to properly identify pixels belonging to granules. Actually, each region contains both pixels related to granules and background. Further refinements have hence to be performed. The first refinement is based on

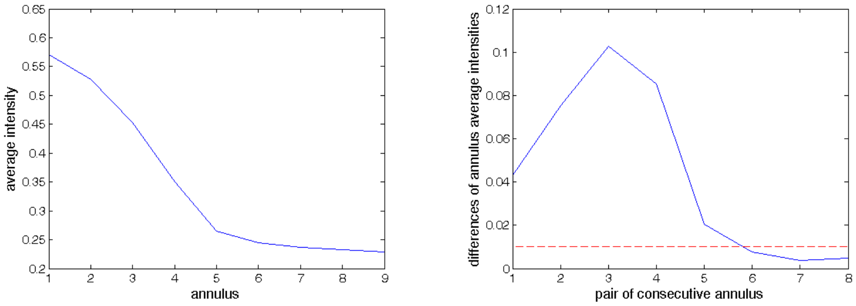

(a) (b)

Figure 5.3: An example of average intensities of concentric annuli (a) and the related differences (b). A red horizontal line is overimposed to represent the adopted threshold.

slope analysis. For each region, several annuli with center located in the related local maximum are considered and their average intensities are computed. This refinement is then performed analyzing the plot of the aforementioned average intensities (see Figure 5.3), considering as granules only the pixels belonging to annuli maintainig a slope value above a fixed threshold.

As can be seen in Figure 5.2(b), some residual pixels belonging to background can still remain after this first refinement. A further step is then performed exploiting Otsu algorithm (Otsu, 1979). This method, starting from the image histogram and considering two classes, computes the optimal threshold that divides them. This threshold is obtained maximizing the inter-class variance. An example of the obtained results is reported in Figure 5.2(c).

## 5.2 Observations and data reduction

In this study we analysed the same dataset used for the analysis of the plasma motion in the light bridge, taken by CRISP on the $6^{th}$ August,

2011. For more details about the dataset, see chapter 4. It consists of the best seeing sequence of the Fe I line at 630.15 nm where the large negative polarity sunspot of the AR NOAA 11263 has been observed.

To study the kinematics of granules in the LB region and in the quiet Sun region, we obtained the Doppler velocity of plasma motions by applying a Gaussian fit to the Fe I line profile at 630.15 nm with the MPFIT routine (Markwardt, 2009) in IDL. The LOS velocity map was calibrated by subtracting the mean velocity of the pixels of a region of quiet Sun in the FOV and by applying the correction due to the convective blueshift. The correction was calculated using the tabulated values from Balthasar (1988).

## 5.3 Results

A map of the continuum intensity of the sunspot observed on August $6^{th}$, 2011, is shown in Figure 4.4. The white boxes in the Northern and in the Southern part of Figure 5.4 indicate the FOV selected to study the physical properties of the solar granulation in the LB (in the following called $FOV_{LB}$) and in the quiet Sun (in the following called $FOV_{QS}$), respectively.

The granulation observed in the $FOV_{LB}$ was identified using the algorithm described in Section 5.1 and using a fixed threshold of 0.01 for the differences of annulus average intensities. The granulation observed in the $FOV_{QS}$ was identified using the same algorithm used for the $FOV_{LB}$, but without any treshold. In Figure 5.5 (*left column*) the two FOVs with their segmentations are shown. The red points identify the maximum continuum intensity of each granule. The two FOVs have the same size of 136 × 46 pixels, corresponding to $8''.01 \times 2''.71$.

The granules which are not located entirely inside each FOV have been omitted from this study. Moreover, we considered only the gran-

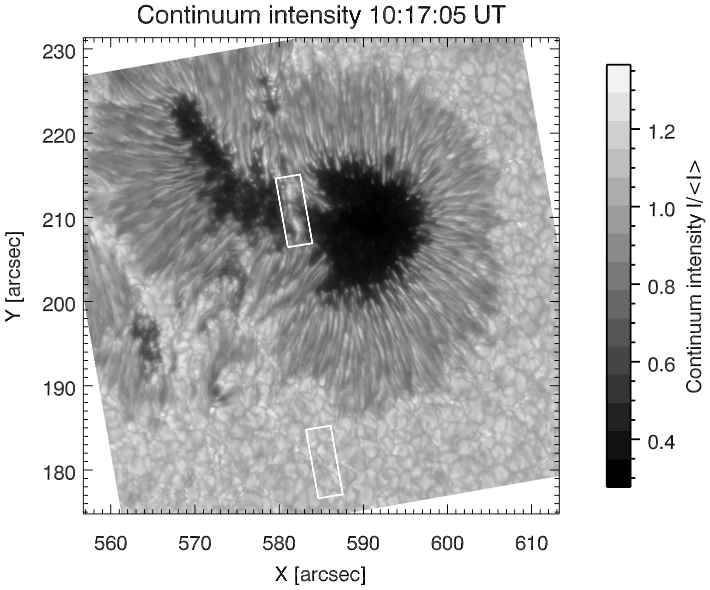

Figure 5.4: Continuum intensity map of the preceding sunspot of AR NOAA 11263 obtained by CRISP in the Fe I 630.15 nm line at 10:17 UT on the August $6^{th}$, 2011. The solid boxes indicate the quiet Sun granulation FOV and the LB granulation FOV analyzed in this study (see text). North is on the top, West is at the right.

ules with a diameter larger than $0\overset{''}{.}18$, which is the spatial resolution of the SST telescope. The diameter of each granule was calculated considering an ideal circular shape of the granule and using the formula: $D = 2(A/\pi)^{1/2}$, where A is the area covered by the pixels corresponding to each granule. The number of granules studied in the $FOV_{LB}$ and in the $FOV_{QS}$ were 41 and 21, respectively. In Figure 5.5 (*right column*) we show the two FOVs where the red points identify the granules that have been selected for this study. The granules without the red point were not considered because they did not fit with the selection criteria. Taking into account that the number of granules is different in each

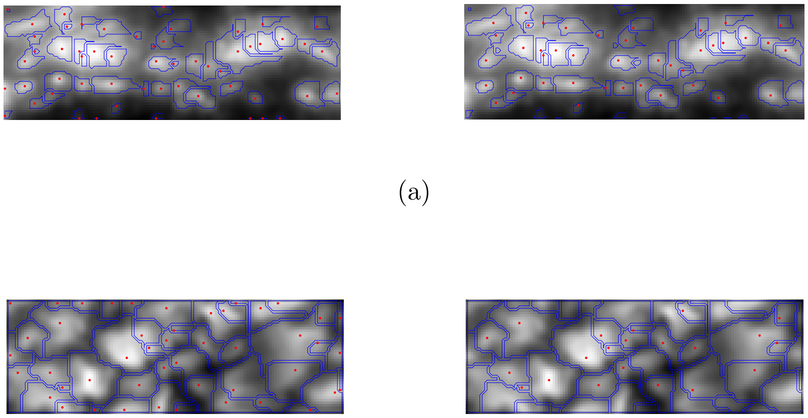

(a)

(b)

Figure 5.5: *Left column*: (a) image of the $FOV_{LB}$ with the segmentation applied to identify the granulation of the LB; (b) image of the $FOV_{QS}$. The red points identify the maximum continuum intensity of each granule. *Right column*: Image of the $FOV_{LB}$ (a) and $FOV_{QS}$ (b) with the segmentation and with the red points which identify only the granules that have been selected for this study.

sample (41 for granules in the $FOV_{LB}$ and 21 for the granules in the $FOV_{QS}$), we consider in the following the normalized values.

In Figure 5.6 (*top left panel*) we show the normalized distribution of the granules diameter studied in the $FOV_{LB}$ (red line) and in the $FOV_{QS}$ (black line). The two plots show that the distribution of the size of the granules in the $FOV_{LB}$ and $FOV_{QS}$ is different. The granules forming the LB are on average smaller than the granules belonging to the quiet Sun region. The range of diameter values for the LB granules is between $0\farcs2$ and $0\farcs6$ (only one granule has a diameter larger than $0\farcs6$), while the range of diameter values for the quiet Sun region is larger and covers values from $0\overset{''}{.}2$ to $1\overset{''}{.}5$. This result confirms the works carried out by Bray et al. (1984) and Brandt (2001).

In Figure 5.6 (*top right panel*) we show the normalized distribution of the mean continuum intensity of the granules studied in the $FOV_{LB}$ (red line) and in the $FOV_{QS}$ (black line). The quiet Sun granules have values of the mean continuum intensity between 0.95 $I_c$ and 1.1 $I_c$, while the mean continuum intensity of the granules in the LB spans between 0.4 $I_c$ and $\sim 1.0$ $I_c$. It is worthy of note that the granulation of the LB shows a wider range of intensity values than in the quiet Sun.

In Figure 5.6 (*bottom central panel*) we show the distribution of the mean Doppler velocity of the granules in the two FOVs. The Doppler velocities of the granules, in the quiet Sun cover a range between $-0.65\,\mathrm{km\,s^{-1}}$ and $+0.65\,\mathrm{km\,s^{-1}}$, showing two peaks centered respectively at $-0.3\,\mathrm{km\,s^{-1}}$ and $0.2\,\mathrm{km\,s^{-1}}$, while the velocity of the granules in the LB is mostly in the range $-0.35\,\mathrm{km\,s^{-1}}$ and $0.15\,\mathrm{km\,s^{-1}}$, and shows that most of them are characterized by upward motion. We stress however that in each granule there are upflow (mostly in the center) and downflow (at the edges) and in Figure 4.6 (*bottom central panel*) we show only the mean value of these motions. The higher upflow motion observed is $-1.2\,\mathrm{km\,s^{-1}}$ and the higher downflow is $1.4\,\mathrm{km\,s^{-1}}$.

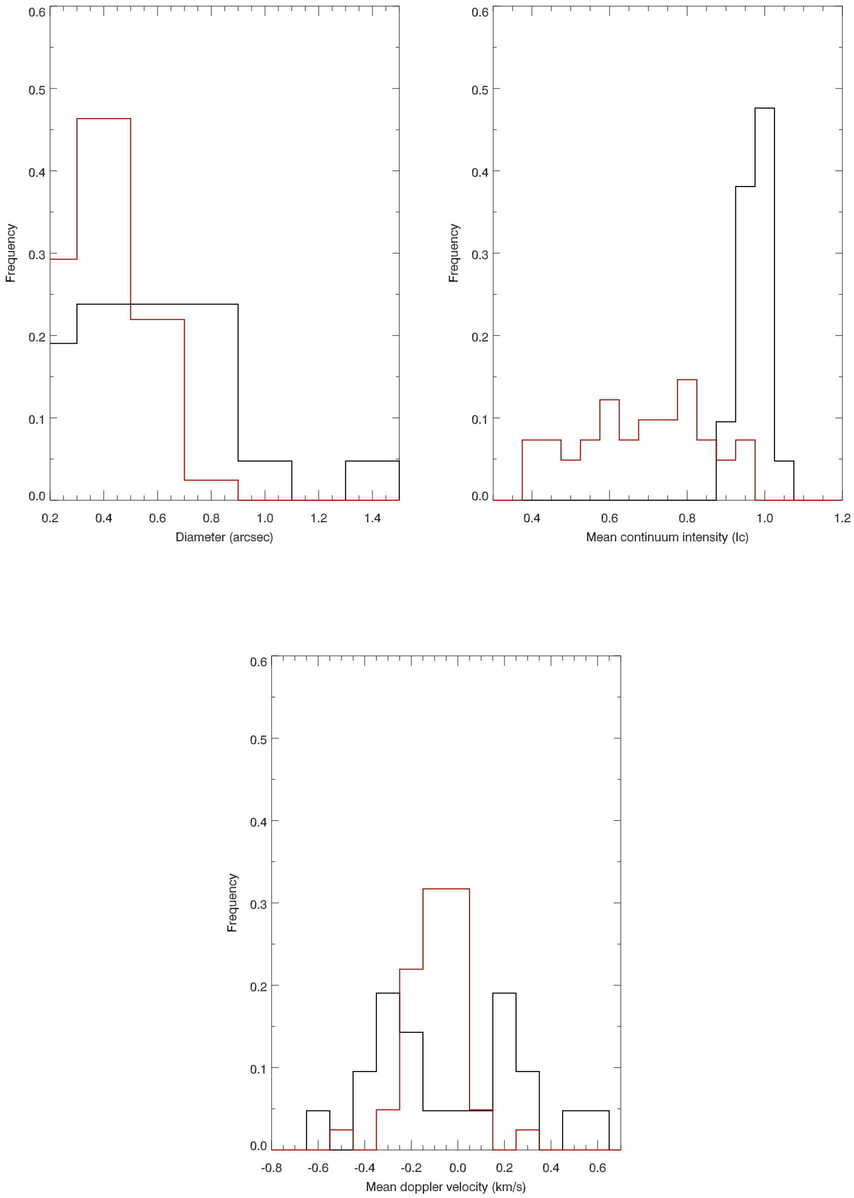

Figure 5.6: Normalized size distribution (*top left panel*), mean continuum intensity (*top right panel*) and mean Doppler velocity (*bottom panel*) of the granules in the $FOV_{LB}$ (red) and in the $FOV_{QS}$ (black).

## 5.4 Discussion

In the last decades, the quiet Sun and its convective motions have been deeply studied thanks to the amount of observations carried out by instruments able to reach high spatial and spectral resolution. However, the properties of the granulation visible in the solar photosphere still need an in-depth study, especially in regions characterized by some peculiar configuration of the surrounding magnetic field, as in the umbra of the sunspots. For this reason we carried out a comparison of size, continuum intensity and Doppler velocity of the granulation in a LB and in the quiet Sun. To reach this goal we used a new identification algorithm for the study of the solar granulation, based on five main steps: a first filtering to reduce the noise of the image, the computation of the local maxima, the segmentation phase and two refinement processes based on slope analysis and on Ostu algorithm. The advantage of this algorithm is its flexibility which allows to measure the properties of granules characterized by different geometry and size, as in our case, where we intend to compare the characteristics of the granulation of the quiet Sun and of the light bridge.

We applied this new algorithm to the best seeing scan of the Fe I line at 630.15 nm taken by CRISP at the SST on August 6th, 2015, when the preceding spot of the AR NOAA 11263 showed a LB. We found significant differences between the two types of granulation.

We found that the diameter of the LB granules was between $0\farcs2$ and $0\farcs6$. These values are lower than the values of the SLBs and higher than the values of the FLBs. Recently, Lagg et al. (2014) observed a strong LB with the granule size comparable with the values of the quiet Sun granulation ($1''$and $2''$). Instead, Sobotka & Puschmann (2009) studied the physical properties of granules in a FLB and found diameters of the granules between $0\farcs13$ and $0\farcs25$, that are lower than the values that we found in our analysis.

The mean continuum intensity of the granules in the LB that we analysed showed a wide range of values between 0.4 $I_c$ and 1.0 $I_c$. In this regard, we recall that Hirzberger et al. (2002) studied the mean continuum intensity of granules in a LB and they found a range of values between 0.8 $\mathrm{I}_c$ and 1.3 $\mathrm{I}_c$. Moreover, they found that the umbral dots analysed in the same FOV had a mean continuum intensity in a range between 0.35 $I_c$ and 0.8 $I_c$ and suggested to use the intensity value of 0.8 $I_c$ to separate the two types of bright structures. It seems however that some granules of the LB that we analyzed have an intensity similar to the typical intensity of the umbral dots.

The Doppler velocities detected in the LB granules ranges between $-0.35\,\mathrm{km\,s^{-1}}$ and $0.15\,\mathrm{km\,s^{-1}}$, with a peak of the frequency distribution at $-0.1\,\mathrm{km\,s^{-1}}$, indicating that most of the LB granules are characterized by upflows.

The Doppler velocity of the quiet Sun granules ranges between $-0.65\,\mathrm{km\,s^{-1}}$ and $0.65\,\mathrm{km\,s^{-1}}$ and show two peaks, centered at $-0.3\,\mathrm{km\,s^{-1}}$ and $0.2\,\mathrm{km\,s^{-1}}$. These values are lower than those previously detected by other authors (see, i.e., Jin et al. (2009); Hirzberger et al. (2002)) and a possible explanation of this discrepancy might be related to a different procedure used to calculate the Doppler velocity (in our analysis this is derived from averaging the Doppler velocity inside each granule).

In conclusion, our analysis shows that the granules of the LB are characterized by a diameter lower than that of the granules of the quiet Sun and that the former have a diameter greater than those of the faint light bridges and lower than those of the strong light bridges. Moreover, the range of intensity of the granules of the LB is typical of the umbral dots and lower than that of the quiet Sun. Finally, the Doppler velocities in the granules of the LB are lower than those of the granules of the quiet Sun and show a peak of the frequency distribution at $-0.1\,\mathrm{km\,s^{-1}}$ (upflow).

# Chapter 6

# Conclusions

In this thesis I reported on the analysis of some phenomena related to the formation and evolution of sunspots in the solar photosphere.

Firstly, I investigated the physical conditions leading to the formation of penumbral filaments around the umbral zone of a sunspot. In literature there are two main models which try to describe the presence of the penumbra in a sunspot. Spruit (1981), Schmidt (1991) and Jahn (1992) proposed a model where the complex magnetic fine structure of the penumbra is due to the convective exchange of flux tubes. According to this model, a flux tube below the penumbra is heated by the field-free convective gas and the heated tube is buoyant and rises (if there is a superadiabatic stratification of the gas below the penumbra). The flux tube at the surface radiates the excess of energy and loses its buoyancy becoming more horizontal and sinking again. The part of the flux tube passing through the solar surface is filled with hot gas and appears bright, while, the other parts of the flux tube lying above the the solar surface appear dark because the gas had time to cool down. Another model proposed to explain the origin of uncombed penumbral filaments was suggested by Wentzel (1992). According to this model, the vertical magnetic flux of the umbra produces a horizontal field component by causing a density inversion with height in the atmospheric layers. A small flux tube is filled up to a certain height and dense material overlies less dense material. The developed Rayleigh-Taylor instability causes the filled flux tube to fall, become horizontal and form the penumbra.

Our observations fit better with this second model: the physical properties of the patches observed around the annular zone indicate that these features may correspond to the footpoints of the field lines of the uncombed configuration that are reclining from the chromosphere to the photosphere.

To obtain a more complete view of the penumbral formation process, new and more accurate observations of this particular phenomenon are necessary, for example to investigate why no brightenings related to a magnetic reconnection process, that changes the magnetic configuration in the annular zone, are observed.

The second investigation concerns the role of the magnetic field in a light bridge formed in a sunspot. LBs are one of the key surface phenomena relating directly to the question of sunspot subsurface structure (Berger & Berdyugina, 2003). Studies of the convective and magnetic characteristics of LBs are useful to discriminate between two classes of sunspot models: the monolithic subsurface magnetic structures (i.e., Knobloch & Weiss (1984)) and the clusters of magnetic flux tubes interspersed with relatively field-free regions (i.e., Parker (1979a); Choudhuri (1992)).

In my analysis (see chapter 4), according to the result obtained by the SIR and Merlin inversions, I found that in the region of the LB, where the magnetic field is lower, convection is more effective and the intensity of the granules of the LB is higher. Therefore, it is possible to conclude that there is convection penetrating from the sub-photospheric layers into a quite field-free gap which is dominating in this LB region.

Moreover, I studied the relation beetween the configuration of the magnetic field in the region surrounding the LB and the plasma motion in the dark lane observed along the LB. The main result obtained in this study is a different plasma motion in the dark lane in two different configurations of the magnetic field (whether vertical or more inclined). More precisely, upflow motions in the dark lane of the LB are observed only in a region where the LB is located between two umbral zones, where the magnetic field is vertical. In the other part of the LB, located between an umbral and a penumbral zone, the upflow motions were much lower. Therefore, the configuration of the magnetic field plays an important role in the LB plasma motions and a more detailed study of this behaviour should be done using high-resolution data to be acquired in future observing campaigns.

The last aspect studied in this thesis deals with a comparison between the physical properties of granules forming a LB and those belonging to the solar granulation in the quiet Sun. During the last years, different kind of algorithms were used to identify every single granule. I used a new algorithm which was able to identify the granules of the quiet Sun and also the smaller ones forming the LB. I found different results of the physical properties of the different granules population and this probably depends on the surrounding regions where the granules are embedded: in the LB region the magnetic field observed is stronger than in the quiet Sun region.

In conclusion, there is much yet to be done to fully understand the interaction between the plasma and the magnetic field in the Sun and the different structures that can be observed on our Star. On the other hand, research must continue its investigation because, even if a model is able to consistently explain what we observe, its validity can be ever denied by new observations. In this respect, observations and explanations of the phenomena that occur in the Sun are really important for the progres of science in all its aspects.

# Bibliography

Asai, A., Ishii, T.T., & Kurokawa, H. 2001, ApJ, 555, L65

Balthasar, H. 1988, Astronomy & Astrophysics, Supplement, 72, 473

Berger, T. E., & Berdyugina, S. V. 2003, ApJ, 589, L117

Berrilli, F., del Moro, D., Florio, A., & Santillo, L. 2005, Sol. Phys., 228, 81

Bharti, L., Joshi, C., Jaaffrey, S. N. A., & Jain, R. 2009, Monthly Notices of the Royal Astronomical Society, 393, 65

Bharti, L., Hirzberger, J., & Solanki, S. K. 2013, A&A, 552, L1

Blanchflower, S. M., Rucklidge, A. M., & Weiss, N. O. 1998, Monthly Notices of the Royal Astronomical Society, 301, 593

Borrero, J. M., & Ichimoto, K. 2011, Living Reviews in Solar Physics, 8, 4

Bovelet, B., & Wiehr, E. 2001, Sol. Phys., 201, 13

Brandt, P. N. 2001, Solar Photosphere: Granulation in Encyclopedia of As- tronomy and Astrophysics, ed. P. Murdin (Bristol, UK: Institute of Physics Publishing, and London, UK: Nature Publishing Group) 2659-2662

Bray, R. J., & Loughhead, R. E. 1964, The International Astrophysics Series, London: Chapman Hall, 1964,

Bray, R. J., & Loughhead, R. E. 1977, Sol. Phys., 54, 319

Bray, R. J., Loughhead, R. E., & Durant, C. J. 1984, Astronomy Express, 1, 39

Bumba, V. 1965, Stellar and Solar Magnetic Fields, 22, 305

Bumba, V., & Suda, J. 1984, Bulletin of the Astronomical Institutes of Czechoslovakia, 35, 28

Cavallini, F., & Reardon, K. 2006, Memorie della Societa Astronomica Italiana Supplementi, 9, 55

Choudhuri, A. R. 1992, NATO Advanced Science Institutes (ASI) Series C, 375, 243

Collados, M., Martinez Pillet, V., Ruiz Cobo, B., del Toro Iniesta, J. C., & Vazquez, M. 1994, A&A, 291, 622

Cowling T.G., 1957, Magnetohydrodynamics, Interscience, New York

Cristaldi, A., Guglielmino, S. L., Zuccarello, F., et al. 2014, ApJ, 789, 162

Culhane, J. L., Harra, L. K., James, A. M., et al. 2007, Sol. Phys., 243, 19

Danielson, R. E. 1964, ApJ, 139, 45

de la Cruz Rodríguez, J., Löfdahl, M. G., Sütterlin, P., Hillberg, T., & Rouppe van der Voort, L. 2015, A&A, 573, AA40

del Toro Iniesta, J. C., Tarbell, T. D., & Ruiz Cobo, B. 1994, ApJ, 436, 400

Falco, M., Borrero, J. M., Guglielmino, S. L., Romano, P., Zuccarello, F., Criscuoli, S., Cristaldi, A., Ermolli, I., Jafarzadeh, S., Rouppe van der Voort, L., 'High-resolution observations of a light bridge in a decaying sunspot', submitted.

Falco, M., Puglisi, G., Guglielmino, S. L., Romano, P., Zuccarello, F., Gallo, G., in progress

Georgoulis, M. K. 2005, ApJ, 629, L69

Gingerich, O., Noyes, R. W., Kalkofen, W., & Cuny, Y. 1971, Sol. Phys., 18, 347

Giordano, S., Berrilli, F., Del Moro, D., & Penza, V. 2008, A&A, 489, 747

Golub, L., Deluca, E., Austin, G., et al. 2007, Sol. Phys., 243, 63

Grossmann-Doerth, U., Schmidt, W., & Schroeter, E. H. 1986, A&A, 156, 347

Hale, G. E. 1908, ApJ, 28, 315

Hirzberger, J., Vázquez, M., Bonet, J. A., Hanslmeier, A., & Sobotka, M. 1997, ApJ, 480, 406

Hirzberger, J., Bonet, J. A., Vázquez, M., & Hanslmeier, A. 1999a, ApJ, 515, 441

Hirzberger, J., Bonet, J. A., Vázquez, M., & Hanslmeier, A. 1999b, ApJ, 527, 405

Hirzberger, J. 2002, A&A, 392, 1105

Hirzberger, J., Bonet, J. A., Sobotka, M., Vázquez, M., & Hanslmeier, A. 2002, A&A, 383, 275

Jurčák, J., Martínez Pillet, V., & Sobotka, M. 2006, A&A, 453, 1079

Lagg, A., Solanki, S. K., van Noort, M., & Danilovic, S. 2014, A&A, 568, A60

Leka, K.D. 1997, ApJ, 484, 900

Leka, K. D., & Skumanich, A. 1998, ApJ, 507, 454

Lemen, J. R., Title, A. M., Akin, D. J., et al. 2012, Sol. Phys., 275, 17

Lites, B.W., Bida, T.A., Johannesson, A., & Scharmer, G.B. 1991, ApJ, 373, 683

Lites B. W., Scharmer G. B., Berger T. E., Title A. M. 2004, Sol. Phys., 221, 65

Lites, B., Casini, R., Garcia, J., & Socas-Navarro, H. 2007, Mem. Societa Astronomica Italiana, 78, 148

Loughhead, R. E., Bray, R. J., & Tappere, E. J. 1979, A&A, 79, 128

Loughhead, R. E., & Bray, R. J. 1961, Australian Journal of Physics, 14, 347

Louis, R.E., Bayanna, A.R., Mathew, S.K., Venkatakrishnan, P. 2008, Sol. Phys., 252, 43

Louis, R.E., Bellot Rubio, L.R., Mathew, S.K., Venkatakrishnan, P. 2009, ApJ, 704, L29

Louis, R. E., Beck, C., & Ichimoto, K. 2014, A&A, 567, A96

Jahn, K. 1992, NATO Advanced Science Institutes (ASI) Series C, 375, 139

Jin, C., Wang, J., & Zhao, M. 2009, ApJ, 690, 279

Jurcák, J., Sobotka, M., & Martínez Pillet, V. 2005, Proceedings of the 11th European Solar Physics Meeting *The Dynamic Sun: Challenges for Theory and Observations* (ESA SP-600). Editors: D. Danesy, S. Poedts, A. De Groof and J. Andries.

Jurcák, J., Martínez Pillet, V., & Sobotka, M. 2006, A&A, 453, 1079

Keppens, R., & Martinez Pillet, V. 1996, A&A, 316, 229

Knobloch, E., & Weiss, N. O. 1984, Monthly Notices of the Royal Astronomical Society, 207, 203

Kosugi, T., Matsuzaki, K., Sakao, T., et al. 2007, Sol. Phys., 243, 3

Markwardt, C. B. 2009, Astronomical Data Analysis Software and Systems XVIII, 411, 251

McIntosh, P. S. 1981, The Physics of Sunspots, 7

Meyer, F., Schmidt, H. U., Weiss, N. O., & Wilson, P. R. 1974, Chromospheric Fine Structure, 56, 235

Muller, R. 1973, Sol. Phys., 32, 409

Muller, R. 1999, Motions in the Solar Atmosphere, 239, 35

Nordlund, Å., & Scharmer, G. B. 2010, in Astrophysics and Space Science Proc., Magnetic Coupling between the Interior and Atmosphere of the Sun, ed. S. S. Hasan & R. J. Rutten (Berlin: Springer), 243

Ortiz, A., Bellot Rubio, L. R., & Rouppe van der Voort, L. 2010, ApJ, 713, 1282

Otsu, N., A threshold selection method from gray-level histograms. IEEE Transactions on Systems, Man and Cybernetics 9, 1, 62-66.

Parker, E. N. 1955, ApJ, 121, 491

Parker, E. N. 1979a, ApJ, 230, 905

Parker, E. N. 1979b, ApJ, 230, 914

Parker, E. N. 1979c, ApJ, 231, 250

Pesnell, W. D., Thompson, B. J., & Chamberlin, P. C. 2012, Sol. Phys., 275, 3

Priest, E. 2014, Magnetohydrodynamics of the Sun, by Eric Priest, Cambridge, UK: Cambridge University Press, 2014,

Reardon, K. P., & Cavallini, F. 2008, A&A, 481, 897

Rempel, M. 2011, ApJ, 729, 5

Rempel, M., & Schlichenmaier, R. 2011, Living Reviews in Solar Physics, 8, 3

Riethmüller, T. L., Solanki, S. K., Zakharov, V., & Gandorfer, A. 2008, A&A, 492, 233

Rimmele T. 1997, ApJ, 490, 458

Rimmele, T. R. 2004, ApJ, 604, 906

Rimmele, T., 2008, ApJ, 672, 684

Romano, P., Frasca, D., Guglielmino, S. L., et al. 2013, ApJ, 771, L3

Romano, P., Guglielmino, S. L., Cristaldi, A., et al. 2014, ApJ, 784, 10

Roudier, T., & Muller, R. 1986, Sol. Phys., 107, 11

Roudier, T., & Muller, R. 1987, Sol. Phys., 107, 11

Rouppe van der Voort, L., Bellot Rubio, L. R., & Ortiz, A. 2010, ApJ, 718, L78

Ruiz Cobo, B., & del Toro Iniesta, J. C. 1992, ApJ, 398, 375

Scharmer, G. B., Pettersson, L., Brown, D. S., & Rehn, J. 1985, Applied Optics, 24, 2558

Scharmer, G. B., Gudiksen, B. V., Kiselman, D., Löfdahl, M. G., & Rouppe van der Voort, L. H. M. 2002, Nature, 420, 151

Scharmer, G. B., Bjelksjo, K., Korhonen, T. K., Lindberg, B., & Petterson, B. 2003, Proc. SPIE, 4853, 341

Scharmer, G. B., Narayan, G., Hillberg, T., et al. 2008, ApJ, 689, L69

Scherrer, P. H., Schou, J., Bush, R. I., et al. 2012, Sol. Phys., 275, 207

Schlichenmaier, R., Rezaei, R., Bello González, N., & Waldmann, T. A. 2010, A&A, 512, L1

Schlusser, M. & Vogler, A., 2006, ApJ, 641, L73

Schmidt, H. U. 1991, Geophysical and Astrophysical Fluid Dynamics, 62, 249

Shimizu, T. 2011, ApJ, 738, 83

Sobotka, M., Bonet, J. A., & Vazquez, M. 1993, ApJ, 415, 832

Sobotka, M., Bonet, J. A., & Vazquez, M. 1994, ApJ, 426, 404

Sobotka, M., Vázquez, M., Bonet, J. A., Hanslmeier, A., & Hirzberger, J. 1999, ApJ, 511, 436

Sobotka, M., & Puschmann, K. G. 2009, A&A, 504, 575

Socas-Navarro, H., Martínez Pillet, V., Sobotka, M., & Vázquez, M. 2004, ApJ, 614, 448

Solanki, S. K., & Montavon, C. A. P. 1993, A&A, 275, 283

Solanki, S. K. 2003, Astronomy and Astrophysics Reviews, 11, 153

Spruit, H. C. 1981, The Physics of Sunspots, 98

Stein, R. F., & Nordlund, A. 1989, ApJ, 342, L95

Stein, R. F., & Nordlund, Å. 1998, ApJ, 499, 914

Strous, L. H. 1995, Helioseismology, 376, 213

Suematsu, Y., Ichimoto, K., Katsukawa, Y., et al. 2007, Bulletin of the American Astronomical Society, 39, 217

Suetterlin, P., & Wiehr, E. 1998, A&A, 336, 367

Tarbell, T. D., Tsuneta, S., & SOT Team 2007, Bulletin of the American Astronomical Society, 39, 217

Thomas, J. H., & Weiss, N. O. 1992, NATO Advanced Science Institutes (ASI) Series C, 375,

Thomas, J. H., Weiss, N. O., Tobias, S. M., & Brummell, N. H. 2002, Nature, 420, 390

Thomas, J. H. & Weiss, N. O., 2004, ARA&A, 42, 517

Tsuneta, S., Ichimoto, K., Katsukawa, Y., et al. 2008, Sol. Phys., 249, 167

van Der Voort, L., Bellot Rubio, L.R., Ortiz, A. 2010, ApJ, 718, L78

van Noort, M., Rouppe van der Voort, L., Lofdahl, M. G. 2005, Sol. Phys., 228, 191

Vaquero, J. M. 2007, Advances in Space Research, 40, 929

Vaquero, J. M., & Vázquez, M. 2009, Astrophysics and Space Science Library, 361,

Vazquez, M. 1973, Solar Phys., 31, 377

Wang, H., & Zirin, H. 1992, Sol. Phys., 140, 41

Watanabe, H., Kitai, R., Ichimoto, K., & Katsukawa, Y. 2009, The Second Hinode Science Meeting: Beyond Discovery-Toward Understanding, 415, 378

Weiss, N. O., Brownjohn, D. P., Matthews, P. C., & Proctor, M. R. E. 1996, Monthly Notices of the Royal Astronomical Society, 283, 1153

Wentzel, D. G. 1992, ApJ, 388, 211

Woods, T., Eparvier, F., Hock, R., et al. 2010, 38th COSPAR Scientific Assembly, 38, 2871

Zwaan, C. 1992, NATO Advanced Science Institutes (ASI) Series C, 375, 75